DETECTION OF POLARIZATION IN THE COSMIC MICROWAVE BACKGROUND USING DASI

J. KOVAC, E. M. LEITCH, C. PRYKE AND J. E. CARLSTROM
University of Chicago, Department of Astronomy & Astrophysics, Department of Physics, Enrico Fermi
Institute, 5640 South Ellis Avenue, Chicago, IL 60637
AND
N. W. HALVERSON AND W. L. HOLZAPFEL
University of California, Department of Physics, Le Conte Hall, Berkeley, CA 94720
Draft version October 30, 2018

ABSTRACT

We report the detection of polarized anisotropy in the Cosmic Microwave Background radiation with the Degree Angular Scale Interferometer (DASI), located at the Amundsen-Scott South Pole research station. Observations in all four Stokes parameters were obtained within two 3°.4 FWHM fields separated by one hour in Right Ascension. The fields were selected from the subset of fields observed with DASI in 2000 in which no point sources were detected and are located in regions of low Galactic synchrotron and dust emission. The temperature angular power spectrum is consistent with previous measurements and its measured frequency spectral index is -0.01 ($-0.16 - 0.14$ at 68% confidence), where 0 corresponds to a 2.73 K Planck spectrum. The power spectrum of the detected polarization is consistent with theoretical predictions based on the interpretation of CMB anisotropy as arising from primordial scalar adiabatic fluctuations. Specifically, E-mode polarization is detected at high confidence (4.9σ). Assuming a shape for the power spectrum consistent with previous temperature measurements, the level found for the E-mode polarization is 0.80 (0.56 – 1.10), where the predicted level given previous temperature data is 0.9 – 1.1. At 95% confidence, an upper limit of 0.59 is set to the level of B-mode polarization with the same shape and normalization as the E-mode spectrum. The TE correlation of the temperature and E-mode polarization is detected at 95% confidence, and also found to be consistent with predictions. These results provide strong validation of the underlying theoretical framework for the origin of CMB anisotropy and lend confidence to the values of the cosmological parameters that have been derived from CMB measurements.

1. INTRODUCTION

Measurements of the Cosmic Microwave Background (CMB) radiation reveal the conditions of the universe when it was $\sim 400,000$ years old with remarkable precision. The three most fundamental properties of the CMB are its frequency spectrum and the angular power spectra of the temperature and polarization fluctuations. The frequency spectrum was well determined by the COBE FIRAS instrument (Mather et al. 1994; Fixsen et al. 1996). The initial detection of temperature anisotropy was made on large angular scales by the COBE DMR instrument (Smoot et al. 1992) and recently there has been considerable progress in measuring the anisotropy on finer angular scales (Miller et al. 1999; Halverson et al. 2002; Netterfield et al. 2002; Lee et al. 2001). There have been many efforts to measure the polarization (see below) but so far, detection of this property of the CMB has remained beyond the reach of the most sensitive observations.

In the past several years, a standard cosmological model has emerged (see, e.g., Hu & Dodelson 2002). In this model, the structure of the CMB angular power spectrum at degree angular scales is assumed to arise from acoustic oscillations of the photon-baryon fluid sourced by primordial scalar adiabatic fluctuations. At decoupling, the modes at maximal amplitude lead to excess power in the observed CMB angular power spectrum resulting in a harmonic series of peaks and troughs. Within this theoretical framework, and given knowledge of the temperature angular power spectrum, a prediction can be made for the level

of the CMB polarization with essentially no free parameters (Kaiser 1983; Bond & Efstathiou 1984; Polnarev 1985; Kamionkowski, Kosowsky, & Stebbins 1997; Zaldarriaga & Seljak 1997; Hu & White 1997; Kosowsky 1999). A determination of the CMB polarization would therefore provide a critical test of the underlying theoretical framework (Hu, Spergel, & White 1997; Kinney 2001; Bucher, Moodley, & Turok 2001) and therefore of the validity of cosmological parameters derived from CMB measurements. Polarization measurements also offer the potential to triple the number of observed CMB quantities and to enhance our ability to constrain cosmological parameters.

CMB polarization arises from Thompson scattering by electrons of a radiation field with a local quadrupole moment (Rees 1968). In the primordial plasma, the local quadrupole moment is suppressed until the photon mean free path grows during decoupling. At this time, the largest contribution to the local quadrupole is due to Doppler shifts induced by the velocity field of the plasma (Zaldarriaga & Harari 1995). In this way, CMB polarization directly probes the dynamics at the epoch of decoupling. For a Fourier mode of the acoustic oscillations, the electron velocities are perpendicular to the wavefronts, leading to either a parallel or perpendicular alignment of the resulting polarization. These polarization modes are referred to as the scalar E-modes in analogy with electric fields; they have no curl component. Since the level of the polarization depends on velocity, one expects that the peaks in the scalar E-mode power spectrum correspond to density modes that are at their highest velocities at

decoupling and are therefore at minimum amplitude. The location of the harmonic peaks in the scalar E-mode power spectrum are therefore expected to be out of phase with the peaks in the temperature spectrum (Kamionkowski et al. 1997; Zaldarriaga & Seljak 1997; Hu & White 1997).

Primordial gravity waves will lead to polarization in the CMB (Polnarev 1985; Crittenden, Davis, & Steinhardt 1993) with an E-mode pattern as for the scalar density perturbations, but will also lead to a curl component, referred to as B-mode polarization (Kamionkowski et al. 1997; Seljak & Zaldarriaga 1997). The B-mode component is due to the intrinsic polarization of the gravity waves. In inflationary models, the level of the gravity wave induced B-mode polarization power is set by the energy scale of inflation to the fourth power. While the detection of B-mode polarization would provide a critical test of inflation, the signal is likely to be very weak and may have an amplitude that is effectively unobservable (Lyth 1997). Furthermore, distortions to the scalar E-mode polarization by the gravitational lensing of the intervening large scale structure in the universe will lead to a contaminating B-mode polarization signal which will severely complicate the extraction of the gravity-wave induced signal (Zaldarriaga & Seljak 1998; Hu & Okamoto 2002; Knox & Song 2002). The possibility, however, of directly probing the universe at energy scales of $\sim 10^{16}$ GeV by measuring the gravity-wave induced polarization (see, e.g., Kamionkowski & Kosowsky 1999) is a compelling goal for CMB polarization observations.

Prior to the results presented in this paper, only upper limits have been placed on the level of CMB polarization. This is due to the low level of the expected signal, demanding sensitive instruments and careful attention to sources of systematic uncertainty (see Staggs, Gunderson, & Church 1999, for a review of CMB polarization measurements).

The first limit to the degree of polarization of the CMB was set by Penzias & Wilson (1965) who stated that the new radiation that they had discovered was isotropic and unpolarized within the limits of their observations. Over the following 20 years, dedicated polarimeters have been used to set much more stringent upper limits on angular scales of order several degrees and larger (Caderni et al. 1978; Nanos 1979; Lubin & Smoot 1979, 1981; Lubin, Melese, & Smoot 1983; Sironi et al. 1997). The current best upper limits for the E-mode and B-mode polarizations on large angular scales are 10 μK at 95% confidence for the multipole range $2 \leq l \leq 20$, set by the POLAR experiment (Keating et al. 2001).

On angular scales of order one degree, Wollack et al. (1993) used the Saskatoon experiment to set the first upper limit to the CMB polarization (25 μK at 95% confidence for $l \sim 75$); this limit is also noteworthy in that it was the first limit that was lower than the level of the CMB temperature anisotropy. The current best limit on similar angular scales was set by the PIQUE experiment (Hedman et al. 2002), who reported a 95% confidence upper limit of 8.4 μK to the E-mode signal, assuming no B-mode polarization. Cartwright et al. (2002) presented a preliminary analysis of CBI data that indicated an upper limit similar to the PIQUE result, but on somewhat smaller scales.

On much finer angular scales of order an arcminute, po-

larization measurements have also been pursued and upper limits set (e.g., Partridge et al. 1997; Subrahmanyan et al. 2000). However, at these angular scales, corresponding to multipoles ~ 5000, the level of the primary CMB anisotropy is strongly damped and secondary effects due to the interactions with large scale structure in the universe are expected to dominate (Hu & Dodelson 2002).

In this paper, we present the results of CMB polarization measurements made with the Degree Angular Scale Interferometer (DASI) located at the NSF Amundsen-Scott South Pole research station during the 2001 and 2002 austral winter seasons. DASI was successfully used to measure the temperature anisotropy from $140 < l < 900$ during the 2000 season. Details of the instrument, the measured power spectrum and the resulting cosmological constraints were presented in a series of three papers (Leitch et al. 2002b; Halverson et al. 2002; Pryke et al. 2002, hereafter Papers, I, II and III, respectively). Prior to the start of the 2001 season, DASI was modified to allow polarization measurements in all four Stokes parameters over the same l range as the previous measurements. The modifications to the instrument, observational strategy, data calibration and data reduction are discussed in detail in Leitch et al. (2002a) (hereafter Paper IV).

This paper is organized as follows. In §2 we briefly summarize the modifications to the instrument, the observing strategy and the data calibration from Paper IV and in §3 the CMB observations and data reduction are discussed. The noise model and detection of signal in our data are discussed in §4. The analysis method is presented in §5 and the results from the likelihood analysis which models and parameterizes the signal in terms of CMB polarization and temperature angular power spectra are given in §6. In §7 we discuss systematic uncertainties including instrumental effects and the possibility of foreground contamination. Conclusions are summarized in §8.

2. MEASURING POLARIZATION WITH DASI

DASI is a compact interferometric array optimized for the measurement of CMB temperature and polarization anisotropy. A detailed discussion of the DASI instrument is given in Paper I and the modifications for polarimetric observations are given in Paper IV. Here we briefly summarize the aspects of the instrument particularly relevant for polarization measurements.

Because they directly sample Fourier components of the sky, interferometers are uniquely suited to measurements of the CMB angular power spectrum. In addition, an interferometer gathers instantaneous two dimensional information while inherently rejecting large-scale gradients in atmospheric emission. For observations of CMB polarization, interferometers offer several additional advantages. They can be constructed with the required small and stable instrumental polarization. Furthermore, linear combinations of the data can be used to construct quantities with essentially pure E- and B-mode polarization response patterns on a variety of scales. This property of the data greatly facilitates the analysis and interpretation of the observed polarization in the context of cosmological models.

DASI consists of 13 horn antennas mounted on a rigid faceplate in a three-fold symmetric pattern. Following

each antenna is a cooled, low-noise HEMT amplifier optimized for the 26 – 36 GHz DASI band. The signals from the receivers are combined in a wideband analog correlator that computes the complex correlation, or *visibilities*, between pairs of receivers in ten 1-GHz bands. The locations of the horns in the faceplate are optimized to provide uniform sampling over the multipole range $l \sim$140 – 900. The DASI mount is designed to track in elevation and azimuth with the additional ability to rotate the entire horn array about the faceplate axis. The flexibility of this mount allows us to tailor the Fourier (u, v) plane coverage of a given observation as well as perform sensitive tests for instrumental offsets and other possible systematic errors.

As was detailed in Paper I and Lay & Halverson (2000), the sky above the South Pole is extremely dry and stable, resulting in atmospheric contamination far below DASI's instrumental noise. In addition to the excellent observing conditions at the Pole, it is possible to track a single field continuously at constant elevation angle. These two characteristics of the Pole enable the deep integrations needed to detect the CMB polarization signal. In these sensitive observations, sources of foreground emission are potentially a serious concern. Fortunately, the sky above the Pole includes regions with low diffuse foreground emission.

2.1. *Hardware Upgrade*

During the 2000–2001 austral summer, DASI's thirteen receivers were retrofit with broadband achromatic circular polarizers. These polarizers employ a multi-element design capable of rejecting the unwanted polarization state to better than 1% across DASI's frequency band (see Paper IV, also §2.3.1).

An interferometer measures the correlations between the signals from pairs of receivers; as indicated by Equation 4 in §5.2, recovery of the full complement of Stokes parameters requires the correlation of all four pairwise combinations of left and right circular polarization states (RR, LL, RL and LR), which we refer to as *Stokes states*. The co-polar states (RR, LL), are sensitive to the total intensity, while the cross-polar states (RL, LR) measure linear combinations of the Stokes parameters Q and U.

Each of DASI's analog correlators can accommodate only a single Stokes state, so measurement of the four combinations is achieved via time-multiplexing. The polarizers for each receiver are switched on a 1-hour Walsh cycle, with the result that over the full period of the cycle, every pair of receivers spends an equal amount of time in all four Stokes states.

2.2. *Gain and Phase Calibration*

In Paper IV, we detail the calibration of the polarized visibilities for an interferometer. In order to produce the calibrated visibilities as defined in Equation 4 below, a complex gain factor G^S which depends on the Stokes state S must be applied to each raw visibility. Although the cross-polar gain factors could easily be determined with observations of a bright polarized source, no suitable sources are known, and we therefore derive the full calibration through observations of an unpolarized source. The gains for a given pair of receivers $m - n$ (a baseline) can be decomposed into antenna-based terms (for example, $G_{mn}^{RL} = g_m^R g_n^{L^*}$), allowing us to construct the cross-

polar gains from g_m^R and g_n^L derived from the co-polar visibilities. DASI's calibration is based on daily observations of the bright HII region RCW38, described at length in Paper I, from which we can determine baseline gains for all Stokes states to better than 2%.

The procedure for deriving the baseline gains from antenna-based terms leaves the cross-polar visibilities multiplied by an undetermined overall phase offset (independent of baseline). This phase offset effectively mixes Q and U, and must be measured to obtain a clean separation of CMB power into E- and B-modes. Calibration of the phase offset requires a source whose polarization angle is known, and we create one by observing RCW38 through polarizing wire grids attached to DASI's thirteen receivers. From the wire-grid observations, we can derive the phase offset in each frequency band with an uncertainty of $\lesssim 0°.4$.

As an independent check of this phase offset calibration, the Moon was observed at several epochs during 2001–2002. Although the expected amplitude of the polarized signal from the Moon is not well known at these frequencies, the polarization pattern is expected to be radial to high accuracy, and this can be used to determine the cross-polar phase offset independently of the wire grid observations. As shown in Paper IV, these two determinations of the phase offset are in excellent agreement.

2.3. *Instrumental Polarization*

2.3.1. *On-Axis Leakage*

For idealized polarizers, the cross-polar visibilities are strictly proportional to linear combinations of the Stokes parameters Q and U. For realistic polarizers, however, imperfect rejection of the unwanted polarization state leads to additional terms in the cross-polar visibilities proportional to the total intensity I. These *leakage* terms are the sum of the complex leakage of the two antennas which form each baseline. Prior to installation on the telescope, the polarizers were tuned to minimize these leakages.

At several epochs during 2001–2002, the antenna-based leakages were determined with a fractional error of 0.3% from deep observations of the calibrator source RCW38. As is shown in Paper IV, antenna-based leakages are $\lesssim 1\%$ (of I) at all frequency bands but the highest, where they approach 2%; this performance is close to the theoretical minimum for this polarizer design. Comparison of the measurements from three epochs separated by many months indicates that the leakages are stable with time.

For observations of the CMB, the presence of leakage has the effect of mixing power from temperature into polarization in the uncorrected visibilities. Given the low level of DASI's leakages, this is expected to be a minor effect at most (see §7). Nonetheless, in the analysis presented in this paper, the cross-polar data have in all cases been corrected to remove this effect using the leakages determined from RCW38.

2.3.2. *Off-Axis Leakage*

Although the polarizers were optimized for low on-axis leakage response, the feeds themselves will induce an instrumental polarization which varies across the primary beam. Offset measurements of RCW38 and the Moon indicate that the off-axis instrumental polarization pattern

is radial, rising from zero at the beam center to a maximum of $\sim 0.7\%$ near $3°$, and then tapering to zero (see also Paper IV).

With the on-axis polarizer leakage subtracted to $\lesssim 0.3\%$ (see above), this residual leakage, while still quite small compared to the expected level of polarized CMB signal (again, see §7), is the dominant instrumental contribution. Although the visibilities cannot be individually corrected to remove this effect (as for the on-axis leakage), it may be incorporated in the analysis of the CMB data. Using fits to the offset data (see Paper IV for details), we account for this effect by modeling the contribution of the off-axis leakage to the signal covariance matrix in the likelihood analysis described in §5.

3. CMB OBSERVATIONS AND DATA REDUCTION

3.1. *Observations*

For the observations presented here, two fields separated by one hour of Right Ascension, at R.A. $= 23^h30^m$ and R.A. $= 00^h30^m$, Dec. $= -55°$, were tracked continuously. The telescope alternated between the fields every hour, tracking them over precisely the same azimuth range so that any terrestrial signal can be removed by differencing. Each 24-hour period comprised 20 hours of CMB observations and 2.3 hours of bracketing calibrator observations, with the remaining time spent on skydips and miscellaneous calibration tasks.

The fields were selected from the 32 fields previously observed by DASI for the absence of any detectable point sources (see Paper I). The locations of the 32 fields were originally selected to lie at high elevation angle and to coincide with low emission in the IRAS 100 micron and 408 MHz maps of the sky (Haslam et al. 1981).

The data presented in this paper were acquired from 2001 April 10 to 2001 October 27, and again from 2002 February 14 to 2002 July 11. In all, we obtained 162 days of data in 2001, and 109 in 2002, for a total of 271 days before the cuts described in the next section.

3.2. *Data Cuts*

Observations are excluded from the analysis, or *cut*, if they are considered suspect due to hardware problems, inadequate calibration, contamination from Moon or Sun signal, poor weather, or similar effects. In §4, we describe consistency statistics that are much more sensitive to these effects than are the actual results of our likelihood analysis, allowing us to be certain that the final results are unaffected by contamination. Here we briefly summarize the principal categories of data cuts; each cut is described in detail in Paper IV.

In the first category of cuts, we reject visibilities for which monitoring data from the telescope indicate obvious hardware malfunction, or simply non-ideal conditions. These include cryogenics failure, loss of tuning for a receiver, large offsets between real/imaginary multipliers in the correlators, and mechanical glitches in the polarizer stepper motors. All data are rejected for a correlator when it shows evidence for large offsets, or excessive noise. An additional cut, and the only one based on the individual data values, is a $> 30\sigma$ outlier cut to reject rare ($\ll 0.1\%$ of the data) hardware glitches. Collectively these cuts reject $\sim 26\%$ of the data.

In the next category, data are cut on the phase and amplitude stability of the calibrator observations. Naturally, we reject data for which bracketing calibrator observations have been lost due to previous cuts. These cuts reject $\sim 5\%$ of the data.

Cuts are also based on the elevation of the Sun and Moon. Co-polar data are cut whenever the Sun was above the horizon, and cross-polar data whenever the solar elevation exceeded $5°$. These cuts reject 8% of the data.

An additional cut, which is demonstrably sensitive to poor weather, is based on the significance of data correlations as discussed in §4.1. An entire day is cut if the maximum correlation exceeds 8σ. A total of 22 days are cut by this test in addition to those rejected by the solar and lunar cuts.

3.3. *Reduction*

Data reduction consists of a series of steps to calibrate and reduce the dataset to a manageable size for the likelihood analysis. Phase and amplitude calibrations are applied to the data based on bracketing observations of our primary celestial calibrator, RCW38. The raw 8.4-s integrations are combined over each 1-hr observation for each of 6240 visibilities (78 complex baselines × 10 frequency bands × 4 Stokes states). Leakage corrections are applied to the data, and sequential observations of the two fields in the same $15°$ azimuth range are differenced to remove any common ground signal. Except in the case of the sum and difference data used for the χ^2 consistency tests in §4.2, observations from different faceplate rotation angles, epochs, and azimuth ranges are combined, as well as the two co-polar Stokes states, LL and RR. The resulting dataset has $N \leq 4680$ elements ($6240 \times 3/4 = 4680$). We call this the uncompressed dataset, and it contains all of the information in our observations of the differenced fields for Stokes parameters I, Q, and U.

4. DATA CONSISTENCY TESTS AND χ^2 RESULTS

We begin our analysis by arranging the data into a vector, considered to be the sum of actual sky signal and instrumental noise: $\boldsymbol{\Delta} = \mathbf{s} + \mathbf{n}$. The noise vector $\mathbf{n}$ is hypothesized to be Gaussian and random, with zero mean, so that the noise model is completely specified by a known covariance matrix $\mathbf{C}_N \equiv \langle \mathbf{nn}^t \rangle$. Any significant excess variance observed in the data vector $\boldsymbol{\Delta}$ will be interpreted as signal. In the likelihood analysis of the next section, we characterize the total covariance of the dataset $\mathbf{C} = \mathbf{C}_T(\kappa) + \mathbf{C}_N$ in terms of parameters κ that specify the covariance $\mathbf{C}_T$ of this sky signal. This is the conventional approach to CMB data analysis, and it is clear that for it to succeed, the assumptions about the noise model and the accuracy of the noise covariance matrix must be thoroughly tested. This is especially true for our dataset, in which we have achieved unprecedented levels of sensitivity in an attempt to measure the very small signal covariances expected from the polarization of the CMB.

4.1. *Noise Model*

The DASI instrument and observing strategy are designed to remove systematic errors through multiple levels of differencing. Slow and fast phase switching as well as field differencing are used to minimize potentially variable

systematic offsets that could otherwise contribute a non-thermal component to the noise. The observing strategy also includes Walsh sequencing of the Stokes states, observations over multiple azimuth ranges and faceplate rotation angles, and repeated observations of the same visibilities on the sky throughout the observing run to allow checks for systematic offsets and verification that the sky signal is repeatable. We hypothesize that after the cuts described in the previous section, the noise in the remaining data are Gaussian and white, with no noise correlations between different baselines, frequency bands, real/imaginary pairs, or Stokes states. We have carefully tested the noise properties of the data to validate the use of this model.

Noise variance in the combined data vector is estimated by calculating the variance in the 8.4-s integrations over the period of 1 hr, before field differencing. To test that this noise estimate is accurate, we compare three different short timescale noise estimates: calculated from the 8.4-s integrations over the 1-hr observations before and after field differencing and from sequential pairs of 8.4-s integrations. We find that all three agree within 0.06% for co-polar data and 0.03% for cross-polar data, averaged over all visibilities after data cuts.

We also compare the noise estimates based on the short timescale noise to the variance of the 1-hr binned visibilities over the entire dataset (up to 2700 1-hr observations, over a period spanning 457 days). The ratio of long timescale to short timescale noise variance, averaged over all combined visibilities after data cuts, is 1.003 for the co-polar data and 1.005 for the cross-polar data, remarkably close to unity. Together with the results of the χ^2 consistency tests described in §4.2, these results demonstrate that the noise is white and integrates down from timescales of a few seconds to thousands of hours. We find that scaling the diagonal noise by 1% makes a negligible difference in the reported likelihood results (see §7).

To test for potential off-diagonal correlations in the noise, we calculate a 6240×6240 correlation coefficient matrix from the 8.4-s integrations for each day of observations. To increase our sensitivity to correlated noise, we use only data obtained simultaneously for a given pair of data vector elements. Due to the variable number of 8.4-s integrations M used to calculate each off-diagonal element, we assess the significance of the correlation coefficient in units of $\sigma = 1/\sqrt{M-1}$. Our weather cut statistic is the daily maximum off-diagonal correlation coefficient significance (see §3.2).

We use the mean data correlation coefficient matrix over all days, after weather cuts, to test for significant correlations over the entire dataset. We find that 1864 (0.016%) of the off-diagonal elements exceed a significance of 5.5σ, when about one such event is expected for uncorrelated Gaussian noise. The outliers are dominated by correlations between real/imaginary pairs of the same baseline, frequency band, and Stokes state, and between different frequency bands of the same baseline and Stokes state. For the real/imaginary pairs, the maximum correlation coefficient amplitude is 0.14, with an estimated mean amplitude of 0.02; for interband correlations the maximum amplitude and estimated mean are 0.04 and 0.003, respectively. We have tested the inclusion of these correlations in the likelihood analysis and find that they have a negligible impact on the results, see §7.

4.2. χ^2 tests

As a simple and sensitive test of data consistency, we construct a χ^2 statistic from various splits and subsets of the visibility data. Splitting the data into two sets of observations that should measure the same sky signal, we form the statistic for both the sum and difference data vectors, $\chi^2 = \mathbf{\Delta}^t \mathbf{C}_N^{-1} \mathbf{\Delta}$, where $\mathbf{\Delta} = (\mathbf{\Delta_1} \pm \mathbf{\Delta_2})/2$ is the sum or difference data vector, and $\mathbf{C}_N = (\mathbf{C}_{N1} + \mathbf{C}_{N2})/4$ is the corresponding noise covariance matrix. We use the difference data vector, with the common sky signal component subtracted, to test for systematic offsets and misestimates of the noise. The sum data vector is used to test for the presence of a sky signal in a straightforward way that is independent of the analysis method used for parameter extraction.

We split the data for the difference and sum data vectors in five different ways:

1. Year – 2001 data vs. 2002 data,

2. Epoch – the first half of observations of a given visibility vs. the second half,

3. Azimuth range – east five vs. west five observation azimuth ranges,

4. Faceplate position – observations at a faceplate rotation angle of 0° vs. a rotation angle of 60°, and

5. Stokes state – co-polar observations in which both polarizers are observing left circularly polarized light (LL Stokes state) vs. those in which both are observing right circularly polarized light (RR Stokes state).

These splits were done on the combined 2001/2002 dataset and (except for the first split type) on 2001 and 2002 datasets separately, to test for persistent trends or obvious differences between the years. The faceplate position split is particularly powerful, since the six-fold symmetry of the (u, v) plane coverage allows us to measure a sky signal for a given baseline with a different pair of receivers, different backend hardware, and at a different position on the faceplate with respect to the ground shields, and is therefore sensitive to calibration and other offsets that may depend on these factors. The co-polar split tests the amplitude and phase calibration between polarizer states, and tests for the presence of circularly polarized light.

For each of these splits, different subsets can be examined: co-polar data only, cross-polar data only (for all except the Stokes state split), various l-ranges (as determined by baseline length in units of wavelength), and subsets formed from any of these which isolate modes with the highest expected signal to noise (s/n). These high s/n (sub)subsets must assume some theoretical signal template in defining the s/n eigenmode basis (Bond, Jaffe, & Knox 1998) in which to arrange the data elements of the original subset, and for this we use the concordance model defined in §5.3, although we find the results are not strongly dependent on choice of model. Note that the definitions of which modes are included in the high s/n subsets are made in terms of average theoretical signal, without any reference to the actual data. In Table 1, we present the difference and sum χ^2 values, for a representative selection

of splits and subsets. In each case we give the degrees of freedom, χ^2 value, and probability to exceed (PTE) this value in the χ^2 cumulative distribution function. For the 296 different split/subset combinations that were examined, the χ^2 values for the difference data appear consistent with noise; among these 296 difference data χ^2's, there are two with a PTE < 0.01 (the lowest is 0.003), one with a PTE > 0.99, and the rest appear uniformly distributed between this range. There are no apparent trends or outliers among the various subsets or splits.

The high s/n mode subsets are more sensitive to certain classes of systematic effects in the difference data vector and more sensitive to the expected sky signal in the sum data vector, that otherwise may be masked by noise. Also, the number of modes with s/n > 1 gives an indication of the expected power of the experiment to constrain the sky signal. The co-polar data, which are sensitive to the temperature signal, have many more high s/n modes than the cross-polar data, which are only sensitive to polarized radiation. Within the context of the concordance model used to generate the s/n eigenmode basis, we have sensitivity with an expected s/n > 1 to ~ 340 temperature (co-polar) modes vs. ~ 34 polarization (cross-polar) modes.

4.3. *Detection of Signal*

Given that the data show remarkable consistency in χ^2 tests of the difference data vectors, the χ^2 values of the sum data vectors can be used to test for the presence of sky signal, independently of likelihood analysis methods described below in §5. In the co-polar data, all splits and subsets show highly significant χ^2 values (PTE $< 1 \times 10^{-16}$, the precision to which we calculate the cumulative distribution function).

For the cross-polar data, the sum data vector χ^2 values for the high s/n subsets show high significance, with the PTE $< 1 \times 10^{-6}$ for all s/n > 1 subsets in Table 1. This simple and powerful test indicates that we have detected, with high significance, the presence of a polarized signal in the data, and that this signal is repeatable in all of the data splits. It should be noted that at this stage in the analysis, the data have not been corrected for the off axis leakage described in Paper IV. In the following likelihood analysis, the off axis leakage is included and shown to have an insignificant impact on the results. The polarization map shown in Figure 1 gives a visual representation of this repeatable polarization signal. Shown are the epoch split sum and difference polarization maps constructed using only the 34 highest s/n modes, as formed in the concordance model s/n eigenmode basis. The sum map shows a repeatable polarized signal, while the difference map is consistent with instrument noise.

The likelihood analysis described in the following sections makes use of all of the information in our dataset. Such an analysis, in principle, may yield statistically significant evidence of a signal even in cases of datasets for which it is not possible to isolate any individual modes which have average s/n > 1. However, the existence of such modes in our dataset, which has resulted from our strategy of integrating deeply on a limited patch of sky, allows us to determine the presence of the signal with the very simple analysis described above. It also reduces sensitivity to the noise model estimation in the likelihood results that we report next. Finally, it gives our dataset

greater power to exclude the possibility of no signal than it might have had if we had observed more modes but with less s/n in each.

5. LIKELIHOOD ANALYSIS FORMALISM

The preceding section gives strong evidence for the presence of a signal in our polarization data. We now quantify the amplitude of that signal using the standard tool of likelihood analysis. In such an analysis, the covariance of the signal, $\mathbf{C}_T(\kappa)$, is modeled in terms of parameters κ appropriate for describing the temperature and polarization anisotropies of the CMB. The covariance of the data vector is modeled $\mathbf{C}(\kappa) \equiv \mathbf{C}_T(\kappa) + \mathbf{C}_N$, where $\mathbf{C}_N$ is the noise covariance matrix. Given our data vector $\mathbf{\Delta}$, the likelihood of the model specified by the parameter vector κ is the probability of our data vector given that model,

$$L(\kappa) = P(\mathbf{\Delta}|\kappa)$$

$$\propto \det(\mathbf{C}(\kappa))^{-1/2} \exp\left(-\frac{1}{2}\mathbf{\Delta}^t \mathbf{C}(\kappa)^{-1} \mathbf{\Delta}\right) \quad (1)$$

Although the full likelihood function itself is the most basic result of the likelihood analysis, it is useful to identify and report the values of the parameters that maximize the likelihood (so-called *maximum likelihood (ML) estimators*). Uncertainties in the parameter values can be estimated by characterizing the shape of the likelihood surface, as discussed further in §5.6.

5.1. *The CMB Power Spectra*

The temperature and polarization anisotropies of the CMB can be characterized statistically by six angular power spectra: three that give the amplitudes of temperature, E-mode and B-mode polarization anisotropies as a function of angular scale, and three that describe correlations between them. These spectra are written C_l^X, with $X = \{T, E, B, TE, TB, EB\}$. In our likelihood analyses, we choose various parameterizations of these spectra to constrain.

For a given cosmological model, these spectra can be readily calculated using efficient, publicly-available Boltzmann codes (Zaldarriaga & Seljak 2000). Details of how to define these spectra in terms of all-sky multipole expansions of the temperature and linear polarization of the CMB radiation field are given by Zaldarriaga & Seljak (1997) and Kamionkowski et al. (1997). For DASI's $3.4°$ field of view, a flat sky approximation is appropriate (White et al. 1999), so that the spectra may be defined somewhat more simply. In this approximation the temperature angular power spectrum is defined

$$C_l^T \simeq C^T(|\mathbf{u}|) \equiv \left\langle \frac{\widetilde{T}^*(\mathbf{u})\,\widetilde{T}(\mathbf{u})}{T_{\mathrm{CMB}}^2} \right\rangle, \quad (2)$$

where $\widetilde{T}(\mathbf{u})$ is the Fourier transform of $T(\mathbf{x})$, T_{CMB} is the mean temperature of the CMB, and $l/2\pi = |\mathbf{u}|$ gives the correspondence between multipole l and Fourier radius $|\mathbf{u}|$. The other spectra in the flat sky approximation are similarly defined, e.g., $C^{TE}(u) \equiv \left\langle \widetilde{T}^*(\mathbf{u})\,\widetilde{E}(\mathbf{u})/T_{\mathrm{CMB}}^2 \right\rangle$. The relationship between $\widetilde{E}, \widetilde{B}$ and the linear polarization Stokes parameters Q and U is

$$\widetilde{Q}(\mathbf{u}) = \cos(2\chi)\,\widetilde{E}(\mathbf{u}) - \sin(2\chi)\,\widetilde{B}(\mathbf{u})$$

$$\widetilde{U}(\mathbf{u}) = \sin(2\chi)\,\widetilde{E}(\mathbf{u}) + \cos(2\chi)\,\widetilde{B}(\mathbf{u}). \quad (3)$$

TABLE 1

χ^2 consistency tests for a selection of data splits and subsets

Temperature Data			Difference		Sum	
Split Type	Subset	# DOF	χ^2	PTE	χ^2	PTE
Year	full	1448	1474.2	0.31	23188.7	$< 1 \times 10^{-16}$
	s/n > 1	320	337.1	0.24	21932.2	$< 1 \times 10^{-16}$
	l range 0–245	184	202.6	0.17	10566.3	$< 1 \times 10^{-16}$
	l range 0–245 high s/n	36	38.2	0.37	10355.1	$< 1 \times 10^{-16}$
	l range 245–420	398	389.7	0.61	7676.0	$< 1 \times 10^{-16}$
	l range 245–420 high s/n	79	88.9	0.21	7294.4	$< 1 \times 10^{-16}$
	l range 420–596	422	410.5	0.65	3122.5	$< 1 \times 10^{-16}$
	l range 420–596 high s/n	84	73.5	0.79	2727.8	$< 1 \times 10^{-16}$
	l range 596–772	336	367.8	0.11	1379.5	$< 1 \times 10^{-16}$
	l range 596–772 high s/n	67	82.3	0.10	991.8	$< 1 \times 10^{-16}$
	l range 772–1100	108	103.7	0.60	444.4	$< 1 \times 10^{-16}$
	l range 772–1100 high s/n	21	22.2	0.39	307.7	$< 1 \times 10^{-16}$
Epoch	full	1520	1546.3	0.31	32767.2	$< 1 \times 10^{-16}$
	s/n > 1	348	366.5	0.24	31430.0	$< 1 \times 10^{-16}$
Azimuth range	full	1520	1542.6	0.34	32763.8	$< 1 \times 10^{-16}$
	s/n > 1	348	355.2	0.38	31426.9	$< 1 \times 10^{-16}$
Faceplate position	full	1318	1415.2	0.03	27446.5	$< 1 \times 10^{-16}$
	s/n > 1	331	365.3	0.09	26270.1	$< 1 \times 10^{-16}$
Stokes state	full	1524	1556.6	0.27	33050.6	$< 1 \times 10^{-16}$
	s/n > 1	350	358.2	0.37	31722.5	$< 1 \times 10^{-16}$
Polarization Data			Difference		Sum	
Split Type	Subset	# DOF	χ^2	PTE	χ^2	PTE
Year	full	2896	2949.4	0.24	2925.2	0.35
	s/n > 1	30	34.4	0.27	82.4	8.7×10^{-7}
	l range 0–245	368	385.9	0.25	315.0	0.98
	l range 0–245 high s/n	73	61.0	0.84	64.5	0.75
	l range 245–420	796	862.2	0.05	829.4	0.20
	l range 245–420 high s/n	159	176.0	0.17	223.8	5.4×10^{-4}
	l range 420–596	844	861.0	0.33	837.3	0.56
	l range 420–596 high s/n	168	181.3	0.23	189.7	0.12
	l range 596–772	672	648.1	0.74	704.4	0.19
	l range 596–772 high s/n	134	139.5	0.35	160.0	0.06
	l range 772–1100	216	192.3	0.88	239.1	0.13
	l range 772–1100 high s/n	43	32.3	0.88	47.6	0.29
Epoch	full	3040	2907.1	0.96	3112.2	0.18
	s/n > 1	34	29.2	0.70	98.6	3.3×10^{-8}
Azimuth range	full	3040	3071.1	0.34	3112.9	0.17
	s/n > 1	34	38.7	0.27	98.7	3.3×10^{-8}
Faceplate position	full	2636	2710.4	0.15	2722.2	0.12
	s/n > 1	32	43.6	0.08	97.5	1.6×10^{-8}

NOTE – tabulated above are χ^2 values for a representative selection of splits and subsets of the combined 2001/2002 dataset. Visibility data containing the same sky signal is split to form two data vectors; the χ^2 statistic is then calculated on both the difference and sum data vectors. Also tabulated are the number of degrees of freedom (# DOF), and probability to exceed (PTE) the value in the χ^2 cumulative distribution function, to show the significance of the result (PTE values indicated as $< 1 \times 10^{-16}$ are zero to the precision with which we calculate the χ^2 cumulative distribution function). Difference data χ^2 values test for systematic effects in the data, while comparisons with sum data values test for the presence of a repeatable sky signal. Temperature (co-polar) data are visibility data in which the polarizers from both receivers are in the left (LL Stokes state) or right (RR Stokes state) circularly polarized state; polarization (cross-polar) data are those in which the polarizers are in opposite states (LR or RL Stokes state). In the temperature data, LL and RR Stokes state data are combined in all but the last type of split. The s/n > 1 subset is the subset of s/n eigenmodes > 1 and the l range high s/n subsets are the 20% highest s/n modes. See §4.2 for further description of the data split types and subsets. We have calculated 296 χ^2 values for various split types and subsets, with no obvious trends that would indicate systematic contamination of the data.
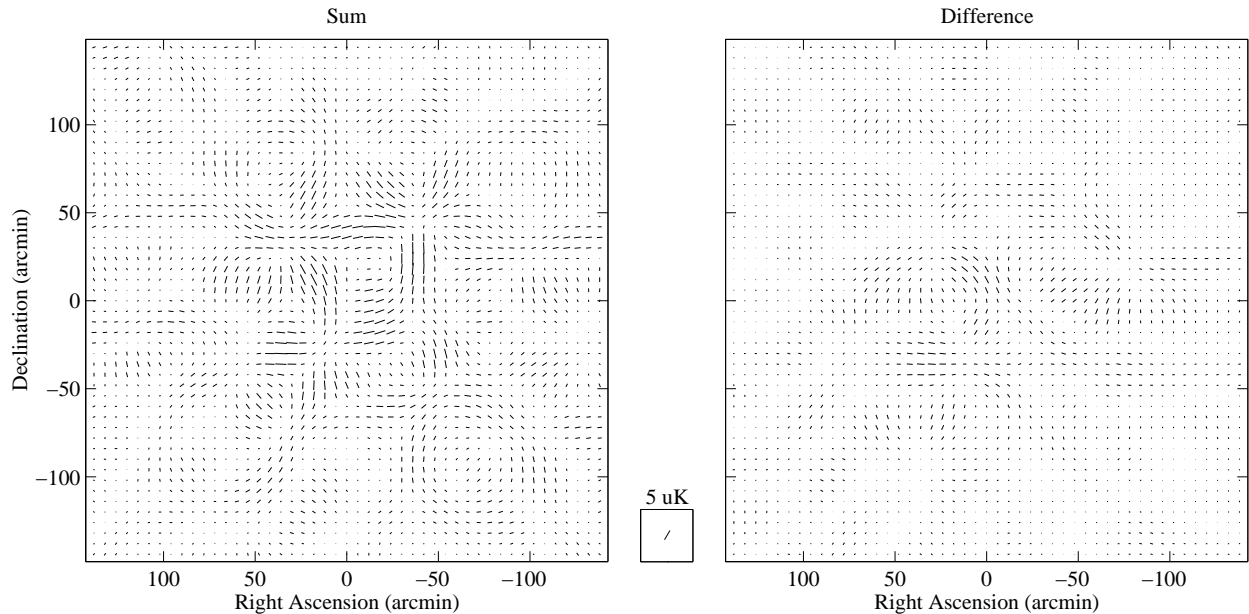
FIG. 1.— Polarization maps constructed from polarized datasets that have been split by epoch, and formed into sum (left) or difference (right) data vectors, as reported in §4.2. In order to isolate the most significant signal in our data, we have used only the subset of 34 eigenmodes which, under the concordance model, are expected to have average signal/noise > 1. Unlike conventional interferometer maps, the signal/noise selected eigenmodes reflect the gain of the primary beam. This is apparent in the difference map (right), which is consistent with noise. Comparison of this map to the sum map (left) illustrates a result also given numerically for this split/subset in Table 1: that these individual modes in the polarized dataset show a significant signal.

where $\chi = \arg(\mathbf{u})$ and the polarization orientation angle defining Q, U are both measured on the sky from north through east.

5.2. Theory Covariance Matrix

The theory covariance matrix is the expected covariance of the signal component of the datavector, $\mathbf{C}_T \equiv \langle \mathbf{s}\mathbf{s}^t \rangle$. The signals measured by the visibilities in our datavector for a given baseline $\mathbf{u}_i$ (after calibration and leakage correction) are

$$V^{RR}(\mathbf{u}_i) = \alpha_i \int d\mathbf{x}\, A(\mathbf{x}, \nu_i) \left[T(\mathbf{x}) + V(\mathbf{x}) \right] e^{-2\pi i \mathbf{u}_i \cdot \mathbf{x}}$$

$$V^{LL}(\mathbf{u}_i) = \alpha_i \int d\mathbf{x}\, A(\mathbf{x}, \nu_i) \left[T(\mathbf{x}) - V(\mathbf{x}) \right] e^{-2\pi i \mathbf{u}_i \cdot \mathbf{x}}$$

$$V^{RL}(\mathbf{u}_i) = \alpha_i \int d\mathbf{x}\, A(\mathbf{x}, \nu_i) \left[Q(\mathbf{x}) + iU(\mathbf{x}) \right] e^{-2\pi i \mathbf{u}_i \cdot \mathbf{x}}$$

$$V^{LR}(\mathbf{u}_i) = \alpha_i \int d\mathbf{x}\, A(\mathbf{x}, \nu_i) \left[Q(\mathbf{x}) - iU(\mathbf{x}) \right] e^{-2\pi i \mathbf{u}_i \cdot \mathbf{x}},$$

$$(4)$$

where $A(\mathbf{x}, \nu_i)$ specifies the beam power pattern at frequency ν_i, $T(\mathbf{x})$, $Q(\mathbf{x})$, $U(\mathbf{x})$, and $V(\mathbf{x})$ are the four Stokes parameters in units of CMB temperature (μK), and $\alpha_i = \partial B_{\mathrm{Planck}}(\nu_i, T_{\mathrm{CMB}}) / \partial T$ is the appropriate factor for converting from these units to flux density (Jy). The co-polar visibilities V^{RR} and V^{LL} are sensitive to the Fourier transform of the temperature signal $T(\mathbf{x})$ and circular polarization component $V(\mathbf{x})$ (expected to be zero). The cross-polar visibilities V^{RL} and V^{LR} are sensitive to the Fourier transform of the linear polarization components Q, U. Using Equation 3, it can be seen that pairwise combinations of the visibilities are direct measures of nearly pure T, E and B Fourier modes on the sky, so

that the dataset easily lends itself to placing independent constraints on these power spectra.

We construct the theory covariance matrix as the sum of components for each parameter in the analysis

$$\mathbf{C}_T(\kappa) = \sum_p \kappa_p \mathbf{B}_T^p. \qquad (5)$$

From Equations $2 - 4$, it is possible to derive a general expression for the matrix elements of a theory matrix component,

$$B_{T\ ij}^p = \frac{1}{2} \alpha_i \alpha_j T_{\mathrm{CMB}}^2 \int d\mathbf{u}\, C^X(u)\, \widetilde{A}(\mathbf{u}_i - \mathbf{u}, \nu_i)$$
$$\times \left[\zeta_1 \widetilde{A}(\mathbf{u}_j - \mathbf{u}, \nu_j) + \zeta_2 \widetilde{A}(\mathbf{u}_j + \mathbf{u}, \nu_j) \right]. \qquad (6)$$

The coefficients ζ_1 and ζ_2 can take values $\{0, \pm 1, \pm 2\} \times \{\cos\{2\chi, 4\chi\}, \sin\{2\chi, 4\chi\}\}$ depending on the Stokes states (RR, LL, RL, LR) of each of the two baselines i and j and on which of the six spectra (T, E, B, TE, TB, EB) is specified by X. The integration may be limited to annular regions which correspond to $l-$ranges over which the power spectrum C^X is hypothesized to be relatively flat, or else some shape of the spectrum may be postulated.

Potentially contaminated modes in the data vector may be effectively projected out using a constraint matrix formalism (Bond et al. 1998). This formalism can be used to remove the effect of point sources of known position without knowledge of their flux densities, as described in Paper II. This procedure can be generalized to include the case of polarized point sources. Although we have tested for the presence of point sources in the polarization power spectra using this method, in the final analysis we use constraint matrices to project point sources out of the temperature data only, and not the polarization data (see §7.2.1).

The off-axis leakage, discussed in §2.3.2 and in detail in Paper IV, has the effect of mixing some power from the temperature signal T into the cross-polar visibilities. Our model of the off-axis leakage allows us write an expression for it analogous to Equation 4, and to construct a corresponding theory covariance matrix component to account for it. In practice, this is a small effect, as discussed in §7.

5.3. *Likelihood Parameters*

In §6 we present the results from nine separate likelihood analyses, organized in three groups: analyses using the polarization (cross-polar) data only, using the temperature (co-polar) data only, and using the full joint temperature and polarization dataset. Our choice of parameters with which to characterize the six CMB power spectra is a compromise between maximizing sensitivity to the signal and constraining the shape of the power spectra. In the different analyses we either characterize various power spectra with a single amplitude parameter covering all angular scales, or split the $l-$range into five bands over which spectra are approximated as piecewise-flat, in units of $l(l+1)C_l/(2\pi)$. Five bands were chosen as a compromise between too many for the data to bear and too few to capture the shape of the underlying power spectra. The $l-$ranges of these five bands are based on those of the nine-band analysis of Paper II; we have simply combined the first four pairs of these bands, and kept the ninth as before. In some analyses we also constrain the frequency spectral indices of the temperature and polarization power spectra as a test for foreground contamination.

The $l-$range to which DASI has non-zero sensitivity is $28 < l < 1047$. That range includes the first three peaks of the temperature power spectrum, and within it the amplitude of that spectrum, which we express in units $l(l+1)C_l/(2\pi)$, varies by a factor of ~ 4. Over this same range, the E-mode polarization spectrum is predicted to have four peaks while rising roughly as l^2 (in the same units), varying in amplitude by nearly two orders of magnitude (Hu & White 1997). The TE correlation is predicted to exhibit a complex spectrum that in fact crosses zero five times in this range.

For the single bandpower analyses which maximize our sensitivity to a potential signal, the shape of the model power spectrum assumed will have an effect on the sensitivity of the result. In particular, if the assumed shape is a poor fit to the true spectrum preferred by the data, the results will be both less powerful and difficult to interpret. For temperature spectrum measurements, the most common choice in recent years has been the so-called flat bandpower, $C_l \propto 1/l(l+1)$, which matches the gross large-scale power law shape of that spectrum. Because of extreme variations predicted in the E and TE spectra over DASI's $l-$range, we do not expect a single flat bandpower parameterization to be a good description of the data. In fact, a more appropriate definition of "flat bandpower" for polarization measurements sensitive to large ranges of $l < 1000$ might be $C_l \propto$ const. Other shapes have been tried, notably the Gaussian autocorrelation function (by the PIQUE group (Hedman et al. 2001)) which reduces to $C_l \propto$ const at large scales and perhaps offers a better fit to the gross amplitude of the predicted E spectrum.

In our single band analyses, we have chosen a shape for our single bandpower parameters based on the predicted spectra for a cosmological model currently favored by observations. The specific model that we choose—which we will call the *concordance model*—is a ΛCDM model with flat spatial curvature, 5% baryonic matter, 35% dark matter, 60% dark energy, and a Hubble constant of 65 km s^{-1} Mpc^{-1}, ($\Omega_b = 0.05, \Omega_{cdm} = 0.35, \Omega_\Lambda = 0.60, h = 0.65$) and the exact normalization $C_{10} = 700\mu K^2$. This concordance model was defined in Paper III as a good fit to the DASI temperature power spectrum and other observations. The concordance model spectra for T, E, and TE are shown in Figure 4. The five flat bandpower likelihood results shown in the same figure, and discussed in the next section, suggest that the concordance shaped spectra do indeed better characterize the data than any power-law approximation. In §6.1.1, we explicitly test the likelihood of the concordance model parameterization against that of the two power laws mentioned above, and find that the concordance model shape is strongly preferred by the data.

It should be noted that the likelihood analysis is always model dependent, regardless of whether a flat or shaped model is chosen for parameterization. To evaluate the expectation value of the results for a hypothesized theoretical power spectrum, one must use window functions appropriate for the parameters of the particular analysis. The calculation of such parameter window functions has been described by Knox (1999), Halverson (2002), and in particular for polarization spectra by Tegmark & de Oliveira-Costa (2001). In general, the parameter window function has a non-trivial shape (even for a flat band-power analysis) which is dependent on the shape of the true spectra as well as the intrinsic sensitivity of the instrument as a function of angular scale. The parameter window functions for the E/B polarization analysis are shown in Figure 2, and are also available on our website[1].

5.4. *Likelihood Evaluation*

Prior to likelihood analysis, the data vector and the covariance matrices can be compressed by combining visibility data from nearby points in the (u, v) plane, where the signal is highly correlated. This reduces the computational time required for the analyses without a significant loss of information about the signal. All analyses were run on standard desktop workstations.

For each analysis, we use an iterated quadratic estimator technique to find the ML values of our parameters (Bond et al. 1998). We also explicitly map out the likelihood function by evaluating Equation 1 over a uniform parameter grid large enough to enclose all regions of substantial likelihood. A single likelihood evaluation typically takes several seconds, so this explicit grid evaluation is impractical for the analyses which include five or more parameters. For each analysis we also implement a Markov chain evaluation of the likelihood function (Christensen et al. 2001). We find this to be a useful and efficient tool for mapping the likelihoods of these high-dimensional parameter spaces in the region of substantial likelihood. We have compared the Markov technique to the grid evaluation for the lower-dimensional analyses and found the results to
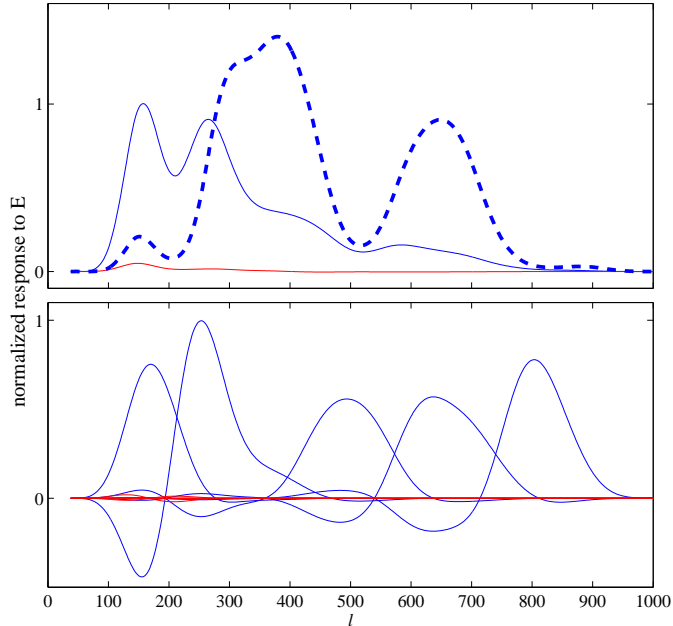
---

[1] http://astro.uchicago.edu/dasi

FIG. 2.— The upper panel shows the E (solid blue) and B (solid red, much lower curve) parameter window functions that indicate the response to the E power spectrum of the two parameters in our E/B analysis. The blue dashed curve shows the result of multiplying the E parameter window function by the concordance E spectrum, illustrating that for this CMB spectrum, most of the response of our experiment's E parameter comes from the region of the second peak ($250 \lesssim l \lesssim 450$), with a substantial contribution also from the third peak and a smaller contribution from the first. The lower panel shows $E1 - E5$ (blue) and $B1 - B5$ (red, again much lower) parameter window functions for the E power spectrum from our $E5/B5$ analysis. DASI's response to E and B is very symmetric, so that the corresponding plots that show these parameters response to the B power spectrum are nearly identical to these, with the E and B parameters reversed.

be in excellent agreement. In all cases, the peak of the full likelihood evaluated with either technique is confirmed to coincide with the ML values returned by the iterated quadratic estimator.

5.5. *Simulations and Parameter Recovery Tests*

The likelihood analysis software was extensively tested through analysis of simulated data. The analysis software and data simulation software were independently authored, as a check for potential coding errors.

Simulated sky maps were generated from realizations of a variety of smooth CMB power spectra, including both the concordance spectrum and various non-concordance models, both with and without E and B polarization and TE correlations. Independent realizations of the sky were "observed" to construct simulated visibilities with Fourier-plane sampling identical to the real data. The simulations were designed to replicate the actual data as realistically as possible and include artifacts of the instrumental polarization response and calibration, such as the on-axis and off-axis leakages described in §2.3, and the cross-polar phase offset described in §2.2, allowing us to test the calibration and treatment of these effects implemented in the analysis software.

Each of the analyses described in §6 was performed on hundreds of these simulated datasets with independent realizations of sky and instrument noise, both with noise variances that matched the real data, and with noise a factor of 10 lower. In all cases, we found that the means of the ML estimators recovered the expectation values $\langle \kappa_p \rangle$ of each parameter without evidence of bias, and that the variance of the ML estimators was found to be consistent

with the estimated uncertainty given by F^{-1} evaluated at $\langle \kappa \rangle$, where F is the Fisher matrix.

5.6. *Reporting of Likelihood Results*

Likelihood results reported in this paper are the global maxima of the multidimensional likelihood functions. Confidence intervals are determined by integrating the likelihood over the full parameter grid, including non-physical values; the reported intervals are the equal-likelihood bounds which enclose 68% of the total probability. This prescription corresponds to what is generally referred to as the *highest posterior density* (HPD) interval. Results for single parameters are obtained by integrating (marginalizing) the likelihood function over the other parameters. In the tabulated results, we also report marginalized uncertainties obtained by evaluating the Fisher matrix at the maximum likelihood model, i.e., $\left(F^{-1}\right)_{ii}^{1/2}$. Although in most cases, the two confidence intervals are quite similar, we regard the HPD interval as the primary result.

For parameters which are intrinsically positive we also marginalize the likelihood distribution after imposing a prior that excludes the unphysical negative values. We then test if the 95% integral point has a likelihood smaller than that at zero; if it does the confidence interval should be regarded as an upper limit rather than a detection and we quote the corresponding value.

5.7. *Goodness-of-Fit Tests*

Using the likelihood function, we wish to determine if our results are consistent with a given model. For example, we would like to know the significance of any detections

and determine if the polarization data are consistent with that predicted in a given cosmological model. We define as a goodness-of-fit statistic the logarithmic ratio of the maximum of the likelihood to its value for some model $\mathcal{H}_0$ described by parameters κ_0.

$$\Lambda(\mathcal{H}_0) \equiv -\log\left(\frac{L\left(\kappa_{ML}\right)}{L\left(\kappa_0\right)}\right).$$

The statistic Λ simply indicates how much the likelihood has fallen from its peak value down to its value at κ_0. Large values indicate inconsistency of the likelihood result with the model $\mathcal{H}_0$. To assess significance, we perform Monte Carlo (MC) simulations of this statistic under the hypothesis that $\mathcal{H}_0$ is true. From this, we can determine the probability, given $\mathcal{H}_0$ true, to obtain a value of Λ that exceeds the observed value, which we hereafter refer to as PTE.

When considering models which the data indicate to be very unlikely, sufficient sampling of the likelihood statistic becomes computationally prohibitive; our typical MC simulations are limited to only 1000 realizations. In the limit that the parameter errors are normally distributed, our chosen statistic reduces to $\Lambda = \Delta\chi^2/2$. The integral over the χ^2 distribution is described by an incomplete gamma function;

$$\mathrm{PTE} = \frac{1}{\Gamma(N/2)}\int_\Lambda^\infty e^{-x}x^{\frac{N}{2}-1}dx$$

where $\Gamma(x)$ is the complete gamma function, and N is the number of parameters. Neither the likelihood function nor the distribution of the ML estimators is, in general, normally distributed, and therefore this approximation must be tested. In all cases where we can compute a meaningful PTE with MC simulations, we have done so and found the results to be in excellent agreement with the analytic approximation. Therefore, we are confident that adopting this approximation is justified. All results for PTE in this paper are calculated using this analytic expression unless otherwise stated.

6. LIKELIHOOD RESULTS

In the following sections we will first discuss analyses based on polarization data only, then those based on temperature data only, and finally joint temperature-polarization analyses. Numerical results for the analyses described in this section are given in Tables 2, 3 and 4. The parameter correlation matrices are tabulated in Appendix A. The conventions used for reporting likelihood results have been discussed in §5.6.

6.1. *Polarization Data Analyses and Results for E and B Parameters*

6.1.1. *E/B Analysis*

The E/B analysis uses two single bandpower parameters to characterize the amplitudes of the E and B polarization spectra. As discussed in §5.3, this analysis requires a choice of shape for the spectra to be parameterized. DASI has instrumental sensitivity to E and B that is symmetrical and nearly independent. Although the B spectrum is not expected to have the same shape as the E spectrum, we choose the same shape for both spectra in order to make the analysis also symmetrical.

We have considered three *a priori* shapes to check which is most appropriate for our data: the concordance E spectrum shape (as defined in §5.3), and two "power law" alternatives, $C_l \propto 1/l(l+1)$ (commonly called "flat") and $C_l \propto \mathrm{const.}$. For each of these three cases, the point at $E = 0, B = 0$ corresponds to the same zero-polarization "nopol" model, so that the likelihood ratios $\Lambda(\mathrm{nopol})$ may be compared directly to assess the relative likelihoods of the best-fit model in each case. For the $C_l \propto 1/l(l+1)$ case, the ML values are $E = 6.8\mu K^2, B = -0.4\mu K^2$, with the log-likelihood at zero falling by $\Lambda(\mathrm{nopol}) = 4.34$. For the $C_l \propto \mathrm{const.}$ case, the ML values are $E = 5.1\mu K^2, B = 1.2\mu K^2$ at $l = 300$, with $\Lambda(\mathrm{nopol}) = 8.48$. For the concordance shape, the ML values are $E = 0.80, B = 0.21$ in units of the concordance E spectrum amplitude, with $\Lambda(\mathrm{nopol}) = 13.76$. The likelihood of the best fit model in the concordance case is a factor of 200 and 12,000 higher than those of the $C_l \propto \mathrm{const.}$ and $C_l \propto 1/l(l+1)$ cases, respectively, and so compared to the concordance shape either of these is a very poor model for the data. The data clearly prefer the concordance shape, which we use for our E/B and other single bandpower analyses.

Figure 3 illustrates the result of this E/B polarization analysis. As stated above, we find that the maximum likelihood value of E is 0.80 with a 68% confidence interval of (0.56 to 1.10). For B, the result should clearly be regarded as a upper limit; 95% of the B > 0 likelihood (marginalized over E) lies below 0.59.

The upper panel of Figure 2 shows the parameter window functions relevant for this analysis. Note that the E parameter has very little sensitivity to B and vice versa —the purity with which DASI can separate these is remarkable. This is also demonstrated by the low correlation (-0.046) between the E and B parameters as determined from the Fisher matrix, as reported in Appendix A.

Assuming that the uncertainties in E and B are normally distributed (§5.6), we estimate the probability that our data are consistent with the zero polarization hypothesis to be $\mathrm{PTE} = 1.05 \times 10^{-6}$. Our data are highly incompatible with the no polarization hypothesis. Marginalizing over B, we find $\Lambda(E = 0) = 12.1$ corresponding to detection of E-mode polarization at a PTE of 8.46×10^{-7} (or a significance of 4.92σ).

The likelihood ratio for the concordance model gives $\Lambda(E = 1, B = 0) = 1.23$, for which the Monte Carlo and analytic PTE are both 0.28. We conclude that our data are consistent with the concordance model.

However, the temperature power spectrum of the CMB is still somewhat uncertain and even within the ~ 7 parameter class of cosmological models often considered, the shape and amplitude of the predicted E-mode spectrum is still somewhat uncertain. To quantify this, we have taken the model grid generated for Paper III and calculated the expectation value of the shaped band E parameter for each model using the window function shown in Figure 2. We then take the distribution of these predicted E amplitudes, weighted by the likelihood of the corresponding model given our previous temperature results (using a common calibration uncertainty for the DASI temperature and polarization measurements). This yields a 68% credible interval for the predicted value of the E parameter of 0.90 to 1.11. Our data are compatible with the expecta-
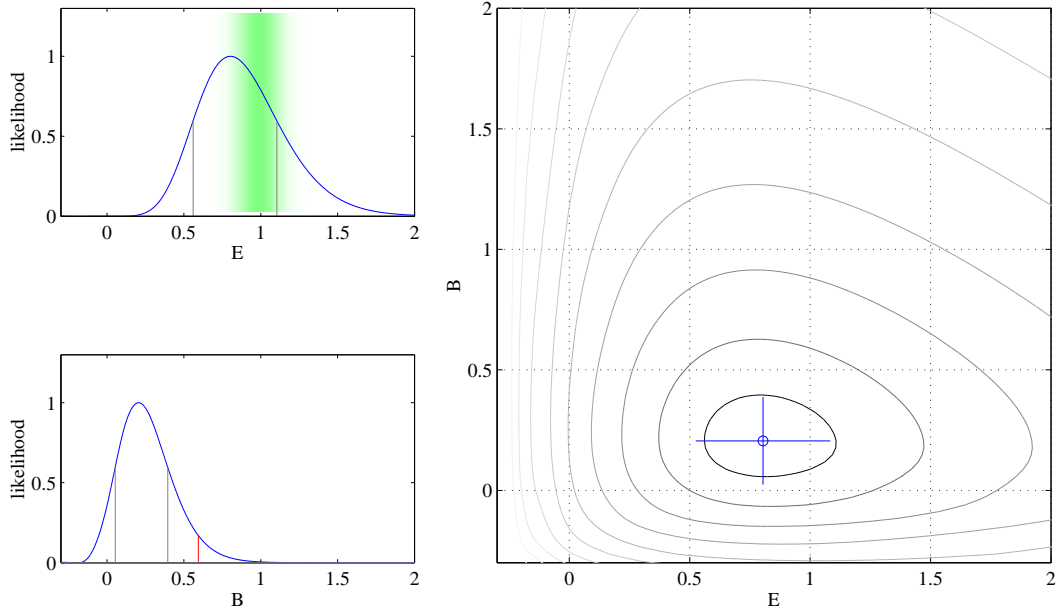
Fig. 3.— Results from the two parameter shaped bandpower E/B polarization analysis assuming an E-mode power spectrum shape as predicted for the concordance model, in units of amplitude relative to that model. The same shape is assumed for the B-mode spectrum. (right panel) The point shows the maximum likelihood value with the cross indicating Fisher matrix errors. Likelihood contours are placed at levels $\exp(-n^2/2)$ relative to the maximum, i.e., for a normal distribution, the extrema of these contours along either dimension would give the marginalized n-sigma interval. (left panels) The corresponding single parameter likelihood distributions marginalized over the other parameter. The grey lines enclose 68% of the total likelihood. The red line indicates the 95% confidence upper limit on B-mode power. The green band shows the distribution of E expectation values for a large grid of cosmological models weighted by the likelihood of those models given our previous temperature result (see Paper III).

tion for E based on existing knowledge of the temperature spectrum.

6.1.2. E/β_E

We have performed a two parameter analysis to determine the amplitude of the E-mode polarization signal as above and the frequency spectral index β_E of this signal relative to CMB (Figure 5). As expected, the results for the E-mode amplitude are very similar to those for the E/B analysis described in the previous section. The spectral index constraint is not strong; the maximum likelihood value is $\beta_E = 0.17$ $(-1.63 - 1.92)$. This result is nevertheless interesting in the context of ruling out possible foregrounds (see §7.2.2 below).

6.1.3. $E5/B5$

The central two panels of Figure 4 show the results of a ten parameter analysis characterizing the E and B-mode spectra using five flat bandpowers for each. The lower panel of Figure 2 shows the corresponding parameter window functions. Note the extremely small uncertainty in the measurements of the first bands $E1$ and $B1$.

Calculating the expectation value for the nominal concordance model in each of the 5 bands yields $E=(0.8,14,13,37,16)$ and $B=(0,0,0,0,0)$ μK^2. At this point in the ten dimensional parameter space, $\Lambda = 5.1$ resulting in a PTE of 0.42, and indicating that our data are consistent with the expected E-mode polarization parameterized in this way. For the no polarization hypothesis, $\Lambda = 15.2$ with a PTE = 0.00073. While still highly inconsistent with no polarization, this statistic is considerably weaker than the equivalent one obtained for the sin-

gle band analysis in §6.1.1, as expected from the increased number of degrees of freedom in this analysis. In this ten dimensional space, the probability under the nopol hypothesis of obtaining a result that is both consistent with the concordance model and inconsistent with nopol is far lower than that of merely obtaining one that is inconsistent with nopol.

6.1.4. $Scalar/Tensor$

Predictions exist for the shape of the E and B-mode spectra which would result from primordial tensor perturbations, although their amplitudes are not well constrained by theory. In a concordance-type model such tensor polarization spectra are expected to peak at $l \sim 100$. Assuming reasonable priors, current measurements of the temperature spectrum (in which tensor and scalar contributions will be mixed) suggest T/S < 0.2 (Wang, Tegmark, & Zaldarriaga 2002), where this amplitude ratio is defined in terms of the tensor and scalar contributions to the temperature quadrupole C_2^T. We use the distinct polarization angular power spectra for the scalars (our usual concordance E shape, with $B = 0$) and the tensors (E_T and B_T) as two components of a likelihood analysis to constrain the amplitude parameters of these components. In principle, because the scalar B-mode spectrum is zero this approach avoids the fundamental sample variance limitations arising from using the temperature spectrum alone. However, the $E5/B5$ analysis (§6.1.3) indicates that we have only upper limit to the E or $B-$mode polarization at the angular scales most relevant ($l \lesssim 200$) for the tensor spectra. It is therefore not surprising that our limits on T/S derived from the polarization spectra as reported in
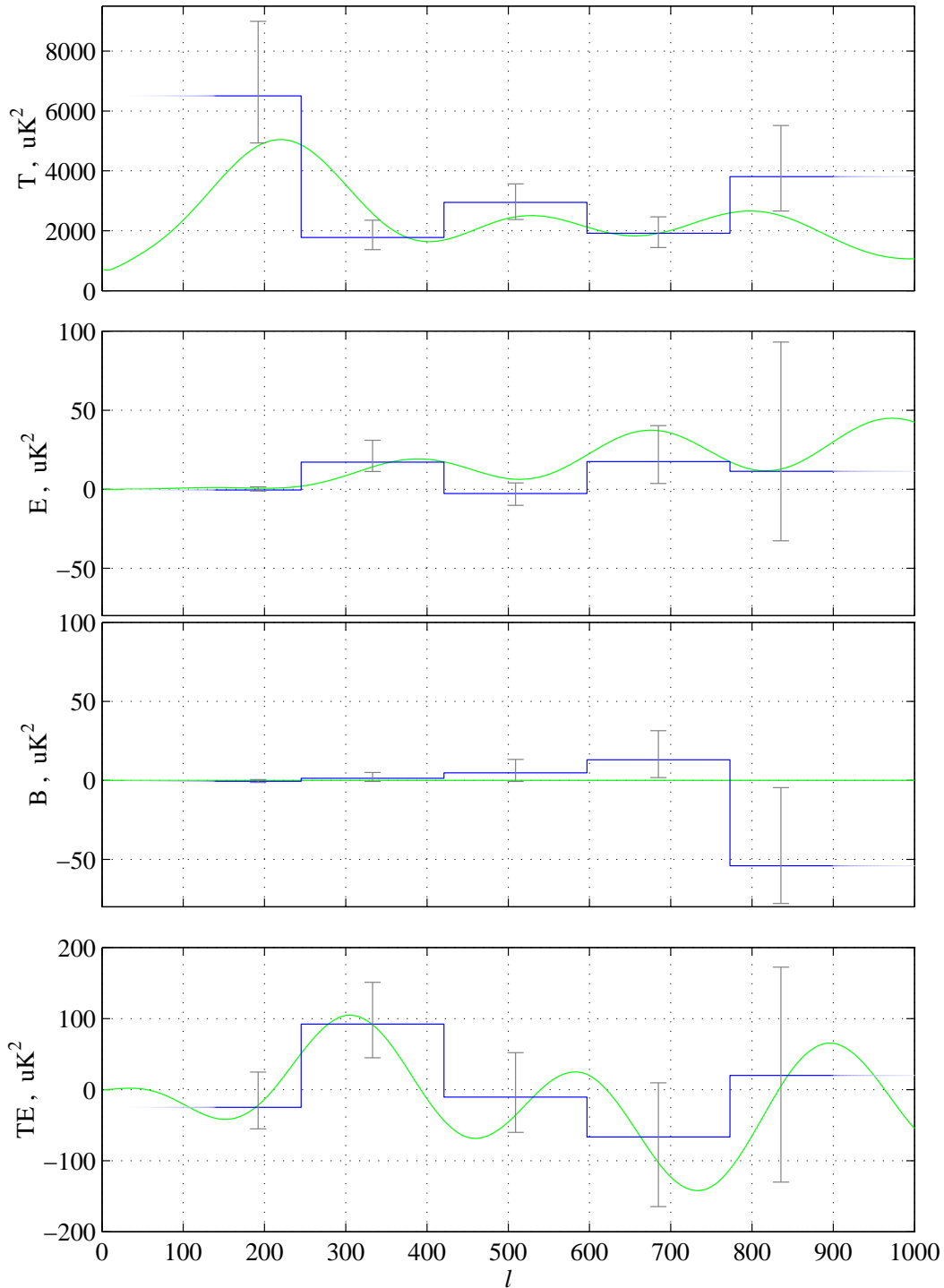
FIG. 4.— Results from several likelihood analyses: The T5 temperature analysis is shown in the top panel. The ten parameter $E5/B5$ polarization analysis is shown in the middle two panels. The 5 TE bands from the $T/E/TE5$ joint analysis are shown in the bottom panel. All the results shown are flat bandpower values. The blue line shows the maximum likelihood bandpower values with the grey error bars indicating the 68% central region of the likelihood marginalizing over the other parameter values (analogous to the grey lines in Figure 3). In each case the green line is the concordance model.

Table 2, are quite weak.

6.2. *Temperature Data Analyses and Results for T Spectrum*

6.2.1. *T/β_T*

Figure 5 shows the results of a two parameter analysis to determine the amplitude and frequency spectral index of the temperature signal. The bandpower shape used is that of the concordance T spectrum, and the amplitude parameter is expressed in units relative to that spectrum. The spectral index is relative to the CMB, so that 0 corre-

TABLE 2
RESULTS OF LIKELIHOOD ANALYSES FROM POLARIZATION DATA

analysis	parameter	$l_{\text{low}} - l_{\text{high}}$	ML est.	$\left(F^{-1}\right)^{1/2}_{ii}$ error	68% interval lower	68% interval upper	U.L.(95%)	units
E/B	E	−	0.80	±0.28	0.56	1.10	−	fraction of concordance E
	B	−	0.21	±0.18	0.05	0.40	0.59	fraction of concordance E
E/β_E	E	−	0.84	±0.28	0.55	1.08	−	fraction of concordance E
	β_E	−	0.17	±1.96	-1.63	1.92	−	temperature spectral index
E5/B5	E1	28 − 245	-0.50	±0.8	-1.20	1.45	2.38	uK^2
	E2	246 − 420	17.1	±6.3	11.3	31.2	−	uK^2
	E3	421 − 596	-2.7	±5.2	-10.0	4.3	24.9	uK^2
	E4	597 − 772	17.5	±16.0	3.8	40.3	47.2	uK^2
	E5	773 − 1050	11.4	±49.0	-32.5	92.3	213.2	uK^2
	B1	28 − 245	-0.65	±0.65	-1.35	0.52	1.63	uK^2
	B2	246 − 420	1.3	±2.4	-0.7	5.0	10.0	uK^2
	B3	421 − 596	4.8	±6.5	-0.6	13.5	17.2	uK^2
	B4	597 − 772	13.0	±14.9	1.6	31.0	49.1	uK^2
	B5	773 − 1050	-54.0	±28.9	-77.7	-4.4	147.4	uK^2
Scalar/Tensor	S	−	0.87	±0.29	0.62	1.18	−	fraction of concordance S
	T	−	-14.3	±7.5	-20.4	-3.9	25.4	T/(S=1)

sponds to a 2.73 K Planck spectrum. The amplitude of T has a maximum likelihood value of 1.19 (1.09 – 1.30), and the spectral index $\beta_T = -0.01$ ($-0.16 - 0.14$). While the uncertainty in the temperature amplitude is dominated by sample variance, the spectral index is limited only by the sensitivity and fractional bandwidth of DASI. Due to the extremely high signal to noise of the temperature data, the constraints on spectral index are superior to those from previous DASI observations (Paper II).

6.2.2. T5

The top panel of Figure 4 shows the results of an analysis using five flat bands to characterize the temperature spectrum. These results are completely dominated by the sample variance in the differenced field. They are consistent with, although less precise than our previous temperature power spectra described in Paper II; we include them here primarily to emphasize that DASI makes measurements simultaneously in all four Stokes parameters and is able to measure temperature as well as polarization anisotropy. Note that these results have not been corrected for residual point sources.

6.3. Joint Analyses and Cross Spectra Results: TE, TB and EB

6.3.1. T, E, TE

Figure 6 shows the results of a three parameter single bandpower analysis of the amplitudes of the T and E spectra, and the TE cross correlation spectrum. As before, bandpower shapes based on the concordance model are used. The T and E constraints are, as expected, very similar to those for the E/B, E/β_E and T/β_T analyses described above. The new result here is TE which has a maximum likelihood value of 0.91 with 68% confidence interval (0.45 to 1.37). Note that in contrast to the two dimensional likelihoods shown in other figures, here we see apparent evidence of correlation between the two pa-

rameters; the parameter correlation coefficients from Appendix A are 0.21 for T/TE and 0.28 for E/TE.

Marginalizing over T and E, we find that the marginalized likelihood on TE peaks very near 1, so that $\Lambda(TE = 1) = 0.02$ with a PTE of 0.857. For the no cross correlation hypothesis, $\Lambda(TE = 0) = 1.85$ with an analytic PTE of 0.054 (the PTE calculated from Monte Carlos is 0.047). This result represents a detection of the expected TE correlation at 95% confidence and is particularly interesting in that it suggests a common origin for the observed temperature and polarization anisotropy.

It has been suggested (Tegmark & de Oliveira-Costa 2001) that an estimator of TE cross correlation constructed using a $TE = 0$ prior may offer greater immunity to systematic errors. We have confirmed that applying such a technique to our data yields similar results to the above likelihood analysis, with errors slightly increased as expected.

6.3.2. T, E, TE5

We have performed a seven parameter analysis using single shaped band powers for T and E, and 5 flat bandpowers for the TE cross correlation; the TE results from this are shown in the bottom panel of Figure 4. In this analysis the B-mode polarization has been explicitly set to zero. Again, the T and E constraints are similar to the values for the other analyses where these parameters appear. The TE bandpowers are consistent with the predictions of the concordance model.

6.3.3. T, E, B, TE, TB, EB

Finally, we describe the results of a six shaped bandpower analysis for the three individual spectra T, E and B, together with the three possible cross correlation spectra TE, TB and EB. We include the B cross-spectra for completeness, though there is little evidence for any B-mode signal. Because there are no predictions for the shapes of
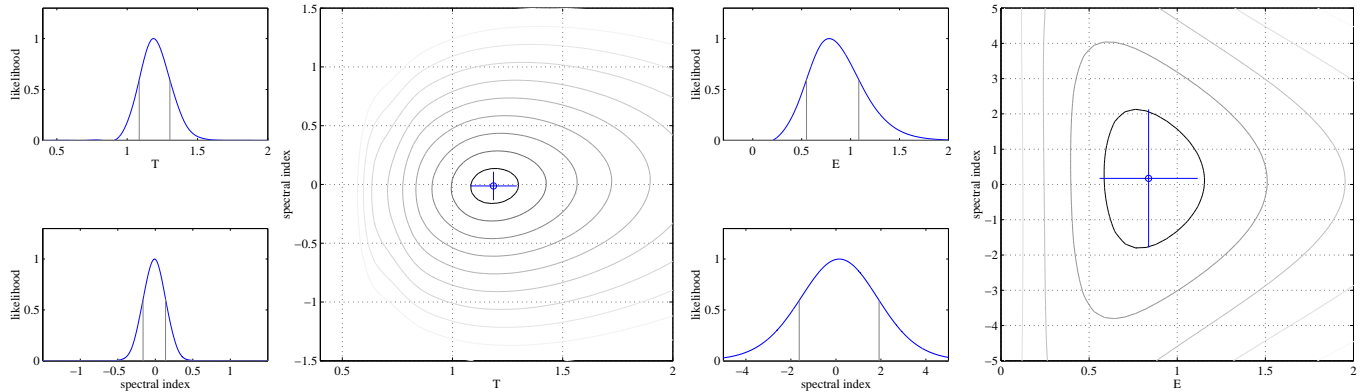
Fig. 5.— (left) Results from the two parameter shaped bandpower T/β_T temperature analysis assuming the T power spectrum shape as predicted for the concordance model, and in units relative to that model. The layout of the plot is analogous to Figure 3. Spectral index is relative to thermal — in these units synchrotron emission would be expected to have an index of approximately -3. (right) Results of the similar E/β_E analysis performed on the polarization data.

TABLE 3
RESULTS OF LIKELIHOOD ANALYSES FROM TEMPERATURE DATA

analysis	parameter	$l_{low} - l_{high}$	ML est.	$\left(F^{-1}\right)^{1/2}_{ii}$ error	68% interval lower	upper	units
T/β_T	T	—	1.19	±0.11	1.09	1.30	fraction of concordance T
	β_T	—	-0.01	±0.12	-0.16	0.14	temperature spectral index
T5	T1	$28 - 245$	6510	±1610	5440	9630	uK^2
	T2	$246 - 420$	1780	±420	1480	2490	uK^2
	T3	$421 - 596$	2950	±540	2500	3730	uK^2
	T4	$597 - 772$	1910	±450	1530	2590	uK^2
	T5	$773 - 1050$	3810	±1210	3020	6070	uK^2

the TB or EB spectra, we preserve the symmetry of the analysis between E and B by simply parameterizing them in terms of the TE and E spectral shapes. The results for T, E, B and TE are similar to as before, with no detection of EB or TB.

7. SYSTEMATIC UNCERTAINTIES

7.1. Noise, Calibration, Offsets and Pointing

In this section, we discuss the effect of systematic uncertainties on the likelihood results. We have repeated each of the nine analyses with alternative assumptions about the various effects which we have identified, and for which there is a well-defined uncertainty. The results of these tests are described below.

Much of the effort of the data analysis presented in this paper has gone into investigating the consistency of the data with the noise model discussed in §4.1. As discussed in that section, we find no discrepancies between complementary noise estimates on different timescales, to a level $\ll 1\%$. As discussed in §4.2, numerous consistency tests on subsets of the co-polar and cross-polar visibility data show no evidence for an error in the noise scaling to a similar level. When we re-evaluate each of the analyses described in §6 with the noise scaled by 1%, the shift in the maximum likelihood values for all parameters is entirely negligible.

In §4.1, we reported the presence of detectable correlations between real/imaginary visibilities and between visibilities from different bands of the same baseline. When these correlations are added to the covariance matrix at the measured level, either separately or together, the effects are again negligible; the largest shift is in the highest-l bin of the E spectrum from the $E5/B5$ analysis (§6.1.3), where the power shifts by $\sim 2\ \mu K^2$.

The absolute cross-polar phase offsets, if uncorrected, will mix power between E and B; these phases have been independently determined from wire-grid calibrations and observations of the Moon, and found to agree to within the measurement uncertainties of $\sim 0°4$ (Paper IV). Reanalysis of the data with the measured phase offsets shifted by $2°$ demonstrates that the likelihood results are immune to errors of this magnitude; the largest effect occurs in the highest-l bin of the TE spectrum from the $T, E, TE5$ analysis (§6.3.2), where the power shifts by $\sim 30\ \mu K^2$.

The on-axis leakages described in §2.3.1 will mix power from T into E and B, and the data are corrected for this effect before input to the likelihood analyses. When these analyses are performed without the leakage correction, the largest effects appear in the shaped TE amplitude analysis (§6.3.1), and the lowest-l bin of $TE5$ from the $T, E, TE5$ analysis (§6.3.2); all shifts are tiny compared to the 68% confidence intervals. As the leakage correction itself has little impact on the results, the uncertainties in the cor-
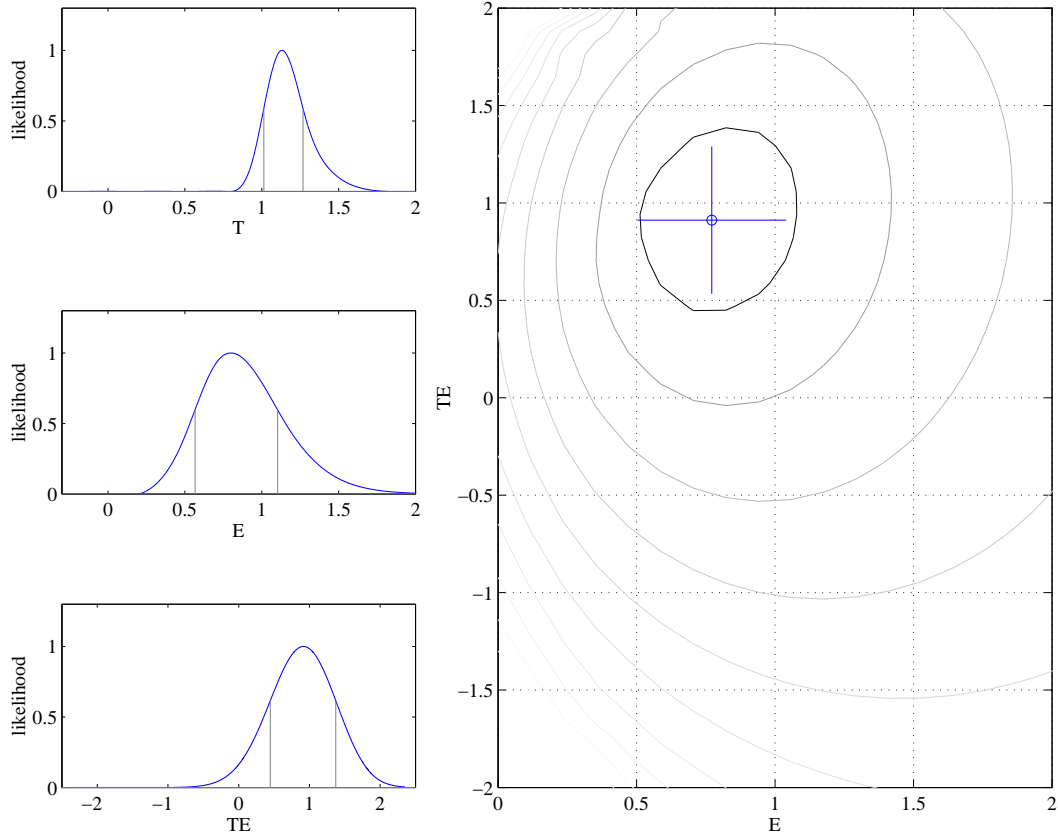
Fig. 6.— Results from the 3 parameter shaped bandpower $T/E/TE$ joint analysis, assuming the spectral shapes as predicted for the concordance model, and in units relative to that model. The layout of the plot is analogous to Figure 3. The two dimensional distribution in the right panel is marginalized over the T dimension.

TABLE 4

RESULTS OF LIKELIHOOD ANALYSES FROM JOINT TEMPERATURE-POLARIZATION DATASET

analysis	parameter	$l_{\rm low} - l_{\rm high}$	ML est.	$\left(F^{-1}\right)_{ii}^{1/2}$ error	68% interval lower	68% interval upper	units
T/E/TE	T	−	1.13	±0.10	1.05	1.29	fraction of concordance T
	E	−	0.77	±0.27	0.57	1.10	fraction of concordance E
	TE	−	0.91	±0.38	0.45	1.37	fraction of concordance TE
T/E/TE5	T	−	1.12	±0.10	1.09	1.31	fraction of concordance T
	E	−	0.81	±0.28	0.71	1.36	fraction of concordance E
	TE1	$28 - 245$	-24.8	±32.2	-55.3	24.7	uK^2
	TE2	$246 - 420$	92.3	±38.4	44.9	151.1	uK^2
	TE3	$421 - 596$	-10.5	±48.2	-60.1	52.0	uK^2
	TE4	$597 - 772$	-66.7	±74.3	-164.6	9.5	uK^2
	TE5	$773 - 1050$	20.0	±167.9	-130.3	172.3	uK^2
T/E/B/TE/TB/EB	T	−	1.13	±0.10	1.03	1.27	fraction of concordance T
	E	−	0.75	±0.26	0.59	1.19	fraction of concordance E
	B	−	0.20	±0.18	0.11	0.52	fraction of concordance E
	TE	−	1.02	±0.37	0.53	1.49	fraction of concordance TE
	TB	−	0.53	±0.32	0.08	0.82	fraction of concordance TE
	EB	−	-0.16	±0.16	-0.38	0.01	fraction of concordance E

rection which are at the $< 1\%$ level will have no noticeable effect.

As described in §2.3.2, the off-axis leakage from the feeds is a more significant effect, and is accounted for in the likelihood analysis by modeling its contribution to the covariance matrix. When this correction is not applied, the E, B results (§6.1.1) shift by $\sim 4\%$ and $\sim 2\%$, respectively, as expected from simulations of this effect. Although this

bias is already a small effect, the simulations show that the correction removes it completely to the degree we understand the off-axis leakage. Uncertainties in the leakage profiles of the order of the fit residuals (see Paper IV) lead to a bias of less than 1%.

The pointing accuracy of the telescope is measured to be better than $2'$ and the rms tracking errors are $< 20''$, as discussed in Papers I and II, this is more than sufficient for the characterization of CMB anisotropy at the much larger angular scales measured by DASI.

Absolute calibration of the telescope was achieved through measurements of external thermal loads, transferred to the calibrator RCW38. The dominant uncertainty in the calibration is due to temperature and coupling of the thermal loads. As discussed in Paper II, we estimate an overall calibration uncertainty of 8% ($1\,\sigma$), expressed as a fractional uncertainty on the C_l bandpowers (4% in $\Delta T/T$). This applies equally to the temperature and polarization data presented here.

7.2. Foregrounds

7.2.1. Point sources

The highest sensitivity point source catalog in our observing region is the 5 GHz PMN survey (Wright et al. 1994). For our first season temperature analysis described in Papers I and II we projected out known sources using this catalog. We have kept to this procedure for the temperature data presented here, projecting the same set of sources as before.

Unfortunately the PMN survey is not polarization sensitive. We note that the distribution of point source polarization fractions is approximately exponential (see below). Total intensity is thus a poor indicator of polarized intensity and it is therefore not sensible to project out the PMN sources in our polarization analysis.

Our polarization fields were selected for the absence of any significant point source detections in the first season data. No significant detections are found in the 2001 – 2002 data, either in the temperature data, which are dominated by CMB anisotropy, or in the polarization data.

To calculate the expected contribution of un-detected point sources to our polarization results we would like to know the distribution of polarized flux densities, but unfortunately no such information exists in our frequency range. However, to make an estimate, we use the distribution of total intensities, and then assume a distribution of polarization fractions. We know the former distribution quite well from our own first season 32-field data where we detect 31 point sources and determine that $dN/dS_{31} = (32 \pm 7)S^{(-2.15\pm0.20)}$ Jy^{-1} Sr^{-1} in the range 0.1 to 10 Jy. This is consistent, when extrapolated to lower flux densities, with a result from the CBI experiment valid in the range 5–50 mJy (Mason et al. 2002). The distribution of point source polarization fractions at 5 GHz can be characterized by an exponential with a mean of 3.8% (Zukowski et al. 1999); data of somewhat lower quality at 15 GHz are consistent with the same distribution (Simard-Normandin, Kronberg, & Neidhoefer 1981b). Qualitatively one expects the polarization fraction of synchrotron-dominated sources to initially rise with frequency, and then plateau or fall, with the break point at frequencies $\ll 5$ GHz (see Simard-Normandin, Kronberg, & Button

(1981a) for an example). In the absence of better data we have conservatively assumed the exponential distribution mentioned above continues to hold at 30 GHz.

We proceed to estimate the effect of point sources by Monte Carlo simulation, generating realizations using the total intensity and polarization fraction distributions mentioned above. For each realization, we generate simulated DASI data by adding a realization of CMB anisotropy and appropriate instrument noise. The simulated data are tested for evidence of point sources and those realizations that show statistics similar to the real data are kept. The effect of off-axis leakage, which is described and quantified in paper IV, is included in these calculations.

When the simulated data are passed through the E/B analysis described in §6.1.1, the mean bias of the E parameter is 0.04 with a standard deviation of 0.05; in 95% of cases the shift distance in the E/B plane is less than 0.13. We conclude that the presence of point sources consistent our observed data have a relatively small effect on our polarization results.

7.2.2. Diffuse Foregrounds

In Paper I, we gave estimates of the total intensity of synchrotron, free-free and thermal dust emission in the region of our fields, showing that the expected amplitudes are very small. This was confirmed in Paper II by a template based cross correlation analysis which showed that the contribution of each of these foregrounds to our temperature anisotropy results were negligible.

The expected fractional polarization of the CMB is of order 10%. The corresponding number for free-free emission is less than 1% and thermal dust emission may be polarized by several percent (see, e.g., Hildebrand et al. 2000). Therefore if free-free and dust emission did not contribute significantly to our temperature anisotropy results they are not expected to contribute to the polarization. Synchrotron emission on the other hand can in principle be up to 70% polarized, and is by far the greatest concern; what was a negligible contribution in the temperature case could be a significant one in polarization.

There are no published polarization maps in the region of our fields. Previous attempts to estimate the angular power spectrum of polarized synchrotron emission have been guided by surveys of the Galactic plane at frequencies of $2 - 3$ GHz (Tegmark et al. 2000). These maps show much more small scale structure in polarization than in temperature, but this is mostly induced by Faraday rotation, an effect which is negligible at 30 GHz. Additionally, since synchrotron emission is highly concentrated in the disk of the Galaxy it is not valid to assume that the angular power spectrum at low Galactic latitudes has much to tell us about that at high.

Our fields lie at Galactic latitude $-58°.4$ and $-61°.9$. The brightness of the IRAS 100 micron and Haslam 408 MHz (Haslam et al. 1981) maps within our fields lie at the 6% and 25% points, respectively, of the integral distributions taken over the whole sky. There are several strong pieces of evidence from the DASI dataset itself that the polarization results described in this paper are free of significant synchrotron contamination. The significant TE correlation shown in Figure 6 indicates that the temperature and E-mode signal have a common origin. The tight constraints on the temperature anisotropy spectral index require that

this common origin has a spectrum consistent with CMB. Galactic synchrotron emission is known to have a temperature spectral index of -2.8 (Platania et al. 1998), with evidence for steepening to -3.0 at frequencies above $1 - 2$ GHz (Banday & Wolfendale 1991). At frequencies where Faraday depolarization is negligible (> 10 GHz), the same index will also apply for polarization. The dramatically tight constraint on the temperature spectral index of 0.01 ($-0.16 - 0.14$) indicates that any component of the temperature signal coming from synchrotron emission is negligibly small in comparison to the CMB. More significantly, the constraint on the E-mode spectral index $\beta_E = 0.17$ ($-1.63 - 1.92$) disfavors synchrotron at nearly 2σ. A third, albeit weaker, line of argument is that a complex synchrotron emitting structure is not expected to produce a projected brightness distribution which prefers E-mode polarization over B-mode. Therefore, the result in Figure 3 could be taken as further evidence that the signal we are seeing is not due to synchrotron emission.

8. CONCLUSION

In this paper, we present the first detection of polarization of the CMB. These results are the product of two years of observations with the DASI telescope within two $3°\!.4$ FWHM fields. For the observations described here, DASI was reconfigured with achromatic polarizers to provide sensitivity in all four Stokes parameters. As described in Paper IV, observations of both polarized and unpolarized astronomical sources give us confidence that the gain and instrumental polarization of the telescope have been precisely characterized.

We have performed extensive consistency tests on various splits and subsets of the visibility data. For those modes expected to have high s/n, a simple comparison of the polarization data with the measured instrumental noise results in a robust detection of a polarized signal with a significance of approximately 5σ. These tests show no indication of systematic contamination and strongly support a celestial origin of the polarized signal. We employ a full likelihood analysis to determine confidence intervals for temperature and polarization models parameterized by shaped and flat band powers. Unlike the DASI temperature angular power spectrum reported in Paper II, the temperature power spectrum presented in this paper is strongly dominated by sample variance. However, the high s/n achieved in the deep polarization presented here permits a precise determination of the spectral index of the CMB temperature anisotropy, $\beta_T = -0.01$ ($-0.16 - 0.14$ at 68% confidence).

A likelihood ratio test is used to demonstrate the agreement of the observed CMB temperature and polarization anisotropy signals with a concordance ΛCDM model, and strongly rejects models without CMB polarization. From this analysis we determine that we have detected E-mode CMB polarization with a significance of 4.9σ. Specifically, assuming a shape for the power spectrum consistent with previous temperature measurements, the level found for the E-mode polarization is 0.80 ($0.56 - 1.10$), where the predicted level given previous temperature data is $0.9 - 1.1$.

The spectral index determined for the observed E-mode polarization signal, $\beta_E = 0.17$ ($-1.63 - 1.92$), is consistent with CMB. At 95% confidence, an upper limit of 0.59 is set to the level of B-mode polarization with the same shape and normalization as the E-mode spectrum. The TE correlation of the temperature and E-mode polarization is detected at 95% confidence, and also found to be consistent with predictions.

We have considered the possibility that our results are contaminated by foreground emission in the form of a distribution of polarized radio point sources and high Galactic latitude synchrotron emission. Simulated distributions of radio sources are shown to contribute insignificant polarization compared to the observed signal. The strongest constraints against diffuse synchrotron emission come from the DASI dataset itself. The observed TE correlation, combined with the precisely thermal spectrum of the temperature anisotropy creates a compelling argument that the E-mode polarization we observe was created at the surface of last scattering. Although the constraint on the E-mode polarization spectral index is not nearly as strong as those for the temperature anisotropy, this result is incompatible with Galactic synchrotron as the source of the observed polarization at nearly 2σ. In general, foregrounds are expected to produce comparable amplitude in both E- and B-mode spectra. Our data therefore provide additional evidence against a strong contribution from foreground emission to the degree that our results limit the ratio of B- to E-mode polarization.

The likelihood results and tests to which we have subjected the data provide self-consistent and strong support for the detection of the polarization induced on the CMB at the surface of last scattering. These results provide strong validation of the underlying theoretical framework for the origin of CMB anisotropy and lend confidence to the values of the cosmological parameters that have been derived from CMB measurements.

ray, in particular Bob Sault and Ravi Subrahmanyan, for their generosity in providing point source observations of the DASI fields.

This research was initially supported by the NSF under a cooperative agreement (OPP 89-20223) with CARA, a NSF Science and Technology Center. It is currently sup-

APPENDIX

LIKELIHOOD CORRELATION MATRICES

Below we tabulate the correlation matrices for our various likelihood analyses to allow the reader to gauge the degree to which each parameter has been determined independently. The covariance matrix is the inverse of the Fisher matrix and the correlation matrix is defined as the covariance matrix normalized such that the diagonal is unity, i.e., $C = F^{-1}$ and $R_{ij} = C_{ij}/\sqrt{C_{ii}C_{jj}}$.

Correlation Coefficient Matrices for 2 Parameter Analyses

E	B		E	β_E		S	T		T	β_T
1	−0.046		1	−0.082		1	−0.339		1	0.023
	1			1			1			1

Correlation Coefficient Matrices for E5/B5 Analysis

E1	E2	E3	E4	E5	B1	B2	B3	B4	B5
1	−0.137	0.016	−0.002	0.000	−0.255	0.047	−0.004	0.000	0.000
	1	−0.117	0.014	−0.002	0.024	−0.078	0.004	0.000	0.000
		1	−0.122	0.015	−0.003	0.010	−0.027	0.003	−0.001
			1	−0.119	0.000	−0.001	0.002	−0.016	0.003
				1	0.000	0.000	0.000	0.002	−0.014
					1	−0.226	0.022	−0.002	0.000
						1	−0.097	0.011	−0.002
							1	−0.111	0.018
								1	−0.164
									1

Correlation Coefficient Matrix for T5 Analysis

T1	T2	T3	T4	T5
1	−0.101	0.004	−0.004	−0.001
	1	−0.092	−0.013	−0.011
		1	−0.115	−0.010
			1	−0.147
				1

Correlation Coefficient Matrix for T/E/TE Analysis

T	E	TE
1	0.017	0.207
	1	0.282
		1

Correlation Coefficient Matrix for T/E/TE5 Analysis

T	E	TE1	TE2	TE3	TE4	TE5
1	0.026	−0.071	0.202	−0.018	−0.075	0.008
	1	−0.067	0.339	−0.023	−0.090	0.008
		1	−0.076	0.006	0.011	−0.001
			1	−0.078	−0.039	0.004
				1	−0.056	0.004
					1	−0.066
						1

Correlation Coefficient Matrix for T/E/B/TE/TB/EB Analysis

T	E	B	TE	TB	EB
1	0.026	0.004	0.230	0.136	0.033
	1	−0.027	0.320	−0.040	−0.182
		1	−0.027	0.219	−0.190
			1	−0.150	0.109
				1	0.213
					1

REFERENCES

Banday, A. J. & Wolfendale, A. W. 1991, MNRAS, 248, 705
Bond, J. R. & Efstathiou, G. 1984, ApJ, 285, L45
Bond, J. R., Jaffe, A. H., & Knox, L. 1998, Phys. Rev. D, 57, 2117
Bucher, M., Moodley, K., & Turok, N. 2001, Physical Review Letters, 87, 191301
Caderni, N., Fabbri, R., Melchiorri, B., et al., 1978, Phys. Rev. D, 17, 1908
Cartwright, J. K., Myers, S. T., Padin, S., et al., 2002, in Moriond Workshop, Vol. XXXVII, The Cosmological Model, in press
Christensen, N., Meyer, R., Knox, L., et al., 2001, Classical and Quantum Gravity, 2677, astro-ph/0103134
Crittenden, R., Davis, R. L., & Steinhardt, P. J. 1993, ApJ, 417, L13
Fixsen, D. J., Cheng, E. S., Gales, J. M., et al., 1996, ApJ, 473, 576
Halverson, N. W. 2002, PhD thesis, Caltech
Halverson, N. W., Leitch, E. M., Pryke, C., et al., 2002, ApJ, 568, 38
Haslam, C. G. T., Klein, U., Salter, C. J., et al., 1981, A&A, 100, 209
Hedman, M. M., Barkats, D., Gundersen, J. O., et al., 2002, ApJ, 573, L73
Hedman, M. M., Barkats, D., Gundersen, J. O., et al., 2001, ApJ, 548, L111
Hildebrand, R. H., Davidson, J. A., Dotson, J. L., et al., 2000, PASP, 112, 1215
Hu, W. & Dodelson, S. 2002, ARA&A, 40, 171
Hu, W. & Okamoto, T. 2002, ApJ, 574, 566
Hu, W., Spergel, D. N., & White, M. 1997, Phys. Rev. D, 55, 3288
Hu, W. & White, M. 1997, New Astron., 2, 323, astro-ph/9706147
Kaiser, N. 1983, MNRAS, 202, 1169
Kamionkowski, M. & Kosowsky, A. 1999, Ann.Rev.Nucl.Part.Sci., 49, 77
Kamionkowski, M., Kosowsky, A., & Stebbins, A. 1997, Phys. Rev. D, 55, 7368
Keating, B. G., O'Dell, C. W., de Oliveira-Costa, A., et al., 2001, ApJ, 560, L1
Kinney, W. H. 2001, Phys. Rev. D, 63, 43001
Knox, L. 1999, Phys. Rev. D, 60, 103516, astro-ph/9902046
Knox, L. & Song, Y. 2002, in 4 pages, 3 figures, submitted to PRL., 2286—+
Kosowsky, A. 1999, New Astronomy Review, 43, 157
Lay, O. P. & Halverson, N. W. 2000, ApJ, 543, 787
Lee, A. T., Ade, P., Balbi, A., et al., 2001, ApJ, 561, L1
Leitch, E. M., Kovac, J. M., Pryke, C., et al., 2002a, ApJ, astro-ph/02
Leitch, E. M., Pryke, C., Halverson, N. W., et al., 2002b, ApJ, 568, 28, astro-ph/0104488
Lubin, P., Melese, P., & Smoot, G. 1983, ApJ, 273, L51
Lubin, P. M. & Smoot, G. F. 1979, Physical Review Letters, 42, 129
—. 1981, ApJ, 245, 1

Lyth, D. H. 1997, Physical Review Letters, 78, 1861
Mason, B. S., Pearson, T. J., Readhead, A. C. S., et al., 2002, ApJ, submitted, astro-ph/0205384
Mather, J. C., Cheng, E. S., Cottingham, D. A., et al., 1994, ApJ, 420, 439
Miller, A. D., Caldwell, R., Devlin, M. J., et al., 1999, ApJ, 524, L1
Nanos, G. P. 1979, ApJ, 232, 341
Netterfield, C. B., Ade, P. A. R., Bock, J. J., et al., 2002, ApJ, 571, 604
Partridge, R. B., Richards, E. A., Fomalont, E. B., et al., 1997, ApJ, 483, 38
Penzias, A. A. & Wilson, R. W. 1965, ApJ, 142, 419
Platania, P., Bensadoun, M., Bersanelli, M., et al., 1998, ApJ, 505, 473
Polnarev, A. G. 1985, Soviet Astronomy, 29, 607
Pryke, C., Halverson, N. W., Leitch, E. M., et al., 2002, ApJ, 568, 46
Rees, M. J. 1968, ApJ, 153, L1
Seljak, U. . & Zaldarriaga, M. 1997, Physical Review Letters, 78, 2054
Simard-Normandin, M., Kronberg, P. P., & Button, S. 1981a, ApJS, 45, 97
Simard-Normandin, M., Kronberg, P. P., & Neidhoefer, J. 1981b, A&AS, 43, 19
Sironi, G., Boella, G., Bonelli, G., et al., 1997, New Astronomy, 3, 1
Smoot, G. F. et al. 1992, ApJ, 396, L1
Staggs, S. T., Gunderson, J. O., & Church, S. E. 1999, in ASP Conf. Ser. 181: Microwave Foregrounds, ed. A. de Oliveira-Costa & M. Tegmark, 299
Subrahmanyan, R., Kesteven, M. J., Ekers, R. D., et al., 2000, MNRAS, 315, 808
Tegmark, M. & de Oliveira-Costa, A. 2001, Phys. Rev. D, 64, 063001
Tegmark, M., Eisenstein, D. J., Hu, W., et al., 2000, ApJ, 530, 133
Wang, X., Tegmark, M., & Zaldarriaga, M. 2002, Phys. Rev. D, 65, 123001
White, M., Carlstrom, J. E., Dragovan, M., et al., 1999, ApJ, 514, 12, astro-ph/9712195
Wollack, E. J., Jarosik, N. C., Netterfield, C. B., et al., 1993, ApJ, 419, L49
Wright, A. E., Griffith, M. R., Burke, B. F., et al., 1994, ApJS, 91, 111
Zaldarriaga, M. & Harari, D. D. 1995, Phys. Rev. D, 52, 3276
Zaldarriaga, M. & Seljak, U. . 1998, Phys. Rev. D, 58, 23003
Zaldarriaga, M. & Seljak, U. 1997, Phys. Rev. D, 55, 1830
—. 2000, ApJS, 129, 431, astro-ph/9911219
Zukowski, E. L. H., Kronberg, P. P., Forkert, T., et al., 1999, A&AS, 135, 571